Updated framework and signal-to-noise analysis of soil mass balance approaches for quantifying enhanced weathering on managed lands

Tim Jesper Suhrhoff[1,2 *], Tom Reershemius[3, 2], Jacob Jordan[4], Shihan Li[5], Shuang Zhang[5], Ella Milliken[2], Boriana Kalderon-Asael[2], Yael Ebert[2], Rufaro Nyateka[2], Christopher T. Reinhard[6], Noah J. Planavsky[2,1]

[1] Yale Center for Natural Carbon Capture, Yale University, New Haven, CT 06511, USA

[2] Department of Earth and Planetary Sciences, Yale University, New Haven, CT 06511, USA

[3] School of Natural and Environmental Sciences, Newcastle University, Newcastle upon Tyne, England NE1 7RU, United Kingdom

[4] Mati Carbon, Houston, TX, USA

[5] Department of Oceanography, Texas A&M University, College Station, TX 77843, USA

[6] School of Earth & Atmospheric Sciences, Georgia Institute of Technology, Atlanta, GA 30332, USA

* corresponding author: timjesper.suhrhoff@yale.edu

Abstract

Enhanced weathering is a promising approach for removing carbon dioxide from the atmosphere at scale while improving agricultural yields. However, accurately quantifying carbon dioxide removal in the field is critical for this approach to scale, particularly given that nearly all of the current deployment activity caters to the voluntary carbon market. Here, we present an updated framework and a signal-to-noise analysis for using soil-based mass balance approaches to quantify rock powder dissolution from field-scale data of soil composition. With additional assumptions, the quantification of rock powder dissolution can be used to estimate carbon dioxide removal potential of EW deployments. The framework we present explicitly accounts for the enrichment of immobile elements in topsoil due to feedstock mass loss and demonstrates that omission of this process systematically overestimates feedstock dissolution. We suggest that the framework should only be used when average post-weathering sample compositions fall within the parameter space representing physically meaningful results (i.e., set out by the mixing relationships between soil, feedstock, and a hypothetical weathered feedstock residue endmember). Building from this, we provide support for the idea that feedstock dissolution should be quantified using the sample population mean rather than individual samples. Given the potential for signal-to-noise issues with

this framework, it is critical that it is utilized only when signals are statistically robust. To illustrate this, we present a signal-to-noise analysis based on a new dataset of soil cation heterogeneity from high-density spatial sampling of 5 fields (0.6-19.2 samples ha^{-1}, 7.1-39.6 pooled cores ha^{-1}). The analysis is based on simulated geolocated sample pairs and suggests that detecting rock powder dissolution via soil mass balance should be feasible when application rates, dissolution fractions, and sampling frequencies are above certain threshold values. When planning deployments, signal emergence can be optimized through careful selection of feedstock composition, strategic feedstock application, and improved sampling protocols.

Synopsis statement: This work advances reliable carbon removal accounting for enhanced weathering by providing a novel tool to quantify rock powder dissolution in soils and demonstrates utility based on a signal-to-noise analysis grounded in new data on in-field soil heterogeneity.

1 Introduction

Achieving the climate targets set out by the Paris agreement requires both deep and immediate emissions cuts as well as the ability to remove emitted carbon from the atmosphere [1–3]. Enhanced Weathering (EW) is one promising approach where CO_2 can be removed from the atmosphere through the reaction with crushed rock feedstocks applied as soil amendments [4–12]. In the ideal case, CO_2 is transferred into bicarbonate and ultimately stored in the oceans for >10 kyrs [13] or stored as carbonate in both soils and deep-sea sediments. This approach has a unique set of advantages including that carbon is stored more durably compared to many biomass-based approaches. Enhanced weathering can also boost crop yields and does not compete for land resources [12,14–16], and the logistics and infrastructure to scale are readily available.

Currently, most CDR activity—including EW—is occurring on the voluntary carbon market [2,17,18]. This means that CDR credits are primarily being used by companies with net-zero goals to balance ongoing emissions. There is a long tradition of tracking soil carbon removal through biogeochemical modeling—foremost with soil organic carbon (e.g., Parton et al., 1998)—and using models for emissions offsetting claims [20,21]. There are also geochemical models for enhanced weathering [22–25]. However, it has been commonly argued that soil biogeochemical models have not progressed or been sufficiently validated to make them fit for offsetting purposes at this stage [26,27]. Therefore, there is a need to develop a suite of tools to track weathering rates at the field scale.

This is a challenge for EW because it is an open-system CDR pathway, and a large number of approaches have been suggested to quantify CDR at the field scale [28,29]. Broadly speaking, Measurement, Reporting, and Verification (MRV) approaches for EW rely on either solid soil, water, gas, or exchangeable phase measurements [28]. Soil-based MRV approaches have a unique set of advantages, namely that they yield a time-integrated signal [28,30], meaning that they resolve all rock feedstock weathering that occurred between different sampling steps without need for high temporal sampling frequencies.

78 One promising variation of soil-based MRV approaches is the use of soil mass balance [28,30,31]. Soil
79 mass balance approaches—here called SOMBA—rely on a sample-resample approach where the
80 dissolution of rock powder feedstock is tied to the loss of cations from mixed soil-feedstock
81 samples. The loss of cations provides an estimate of feedstock dissolution, and with additional
82 assumptions can be translated into an estimate of initial CDR. Here, we present an updated
83 framework for this approach that explicitly considers the impact of immobile element enrichment
84 in soils due to feedstock mass loss. Furthermore, we demonstrate some of the intricacies of this
85 approach, perform a signal-to-noise analysis, and share tools to help users constrain rock powder
86 dissolution in their own field deployments. The signal-to-noise analysis is grounded in a new
87 dataset (5 fields, 998 total samples) where spatial heterogeneity in soil major and trace elemental
88 concentration is assessed at a high spatial sampling density.
89

2 Soil mass balance framework

Soil mass balance approaches assume that mobile base cations are lost from the solid phase of the soil-feedstock mixture during feedstock dissolution, while immobile elements are retained in the solid phase of the soil. Base cations mobilized during feedstock dissolution can be temporarily retained on the soil exchange complex [26,32,33], but these can also be readily quantified. Using these assumptions, practitioners can calculate weathering rates of feedstock material based on the mobility of base cations relative to immobile elements [34–46]. In the context of EW, this framework was first applied in 2023 [30,47] and has since been built upon in several publications [12,28,31,48,49] and preprints [50,51].

For this approach to be effective, rock feedstock added to fields must be enriched in base cations compared to background soil. If immobile element abundance is also being used to evaluate the amount of feedstock, at least one immobile element needs to be enriched. If these conditions are met, the enrichment of immobile elements in topsoils can be used to constrain rock powder addition, and the loss of cations can be used to estimate rock powder dissolution. If these conditions are not met, SOMBA are not suitable to detect CDR through EW [28,30,31]. Using an immobile element to constrain rock powder addition has the benefit that rock powder loss through, e.g., erosion, is not erroneously detected as weathering, as may be the case if only changes in base cation concentration are considered. Because first applications of this approach to EW have used Ti as the proxy for rock powder addition, this approach has also been called "TiCAT" [30], but because other immobile elements may be used [31], we now refer to this approach more broadly as SOMBA.

The loss of cations from topsoils upon weathering can be used to constrain the fraction of rock powder that has dissolved. This in turn can be a proxy for CDR, but translating rock powder dissolution into CDR estimates requires additional assumptions as well as quantification of downstream loss processes [28,30]. These are discussed in detail elsewhere [28,52–54] and are beyond the scope of this study. Our focus here is to present an updated framework for the quantification of rock powder dissolution, as well as a signal-to-noise analysis of the utility of this approach against

background soil heterogeneity. We also share the accompanying code to provide future ERW deployments with a solid foundation for the quantification of rock powder dissolution.

2.1 Calculation of feedstock dissolution fraction

After rock powder that has an elevated base cation content (*[j]*, with the square brackets denoting concentrations per mass of feedstock) and is enriched in at least one immobile element (*[i]*) is added to fields, the composition of the initial soil-feedstock mixture falls onto a mixing line between the soil and feedstock endmembers (Figure 1a). As the rock powder dissolves, mobile base cations are leached from the mineral phase. This loss of cations is used to quantify the fraction of rock powder that has weathered. This estimate of base cation loss reflects the dissolution of primary feedstock when a chemical extraction of secondary phases or exchangeable cations is performed prior to analysis. Alternatively, the estimate can reflect the proportion of the overall feedstock base cation inventory that has been leached from topsoils entirely if bulk samples are used.

Enrichment of immobile elements through rock powder dissolution occurs when they are retained in topsoil while a soluble fraction of feedstock is lost from the system. Assuming that the topsoil volume sampled does not change and that there is no change in porosity, lost feedstock in a sample is replaced with soil that also contains immobile elements in addition to the retained immobile elements added via the rock powder. Furthermore, if the density of feedstock is greater than that of soil, as is true for most cases, this means that the mass being used to calculate the concentration *[i]* is less than for the initial soil-feedstock mixture, such that $[i]_{t=n} > [i]_{t=0}$ in all cases where feedstock is partially dissolved. As a result of cation loss and immobile element enrichment, the soil-feedstock mixture composition is evolving from the pre-weathering composition on the mixing line along a vector towards the bottom right in *[j]* vs. *[i]* space (Figure 1b).

One way to calculate the dissolution fraction (here denoted as the mass transfer coefficient τ_j, used synonymously to dissolution fraction in this manuscript) is from the loss of cations compared to the pre-weathering soil-feedstock mix:

$$\tau_j = \frac{\Delta[j]}{[j]_{add}} \quad (1)$$

$$[j]_{add} = [j]_0 - [j]_s \quad (2)$$

where $[j]_{add}$ is the increase in base cation concentrations due to the addition of rock powder, $\Delta[j]$ reflects the decrease of base cation concentrations due to feedstock dissolution, and the subscript *s* corresponds to baseline soil. If the effect of immobile element enrichment is not taken into account, and the fraction of feedstock in the pre-weathering soil-feedstock mix and associated cation addition is calculated simply by vertically projecting the post-weathering composition onto the mixing line (Figure 1c), the estimate of the cations lost from topsoils ($\Delta[j]^*$) is inflated, such that the erroneous estimate τ_j^* would be larger than τ_j. The impact of this enrichment process on post-weathering soil concentrations as well as estimates of the fraction of feedstock that has dissolved is discussed in section 3.1.

An alternative way to calculate the fraction of rock powder that has dissolved without exact knowledge of the pre-weathering soil-feedstock mix composition is to describe the post-weathering composition as a mix of three endmembers: pure soil, pure feedstock, as well as the composition of a hypothetical weathered feedstock residue endmember (Figure 1d). The composition of this hypothetical endmember is defined to be the composition that a layer of soil would have after a layer of pure feedstock (corresponding to the soil sampling depth, d_{sample}) has dissolved. Assuming mass and volume conservation, this endmember mixing approach can be described by a system of equations such that each endmember contributes a volume proportion (X) to the observed post-weathering composition, which together sum to unity:

$$X_s + X_f + X_{wf} = 1 \quad (3)$$

Where subscripts *s*, *f*, and *wf* correspond to baseline soil, feedstock, and weathered feedstock. Because in practical field sampling based on constant soil sampling depths, a system of constant *volume* is sampled, these endmember contributions reflect *volume* contributions to the sampled soil volume defined by the sampling depth over a given area (all calculations and code shared here use 1 hectare (ha) by default). The endmember contributions reflect three unknowns. Hence, we

set up two additional equations reflecting mass conservation of immobile elements as well as mobile base cations respectively.

$$[j]_s X_s \rho_s + [j]_f X_f \rho_f + [j]_{wf} X_{wf} \rho_{wf} = [j]_{mix,t=n}(X_s \rho_s + X_f \rho_f + X_{wf} \rho_{wf}) \quad (4)$$

$$[i]_s X_s \rho_s + [i]_f X_f \rho_f + [i]_{wf} X_{wf} \rho_{wf} = [i]_{mix,t=n}(X_s \rho_s + X_f \rho_f + X_{wf} \rho_{wf}) \quad (5)$$

Where ρ_i is the density of each respective endmember. Note that it is important to account for the impact of immobile element enrichment due to mass loss also for the composition of the hypothetical weathered feedstock endmember. These equations can be solved (see S1.1 for detailed derivation) to calculate the contribution of each endmember to the observed post-weathering composition:

$$X_f = \frac{\rho_s([j]_{mix,t=n} - [j]_s)}{\rho_s([j]_{mix,t=n} - [j]_s) - \rho_f([j]_{mix,t=n} - [j]_f)} \quad (6)$$

$$X_{wf} = \frac{\rho_s([j]_{mix,t=n} - [j]_s)\rho_f([i]_{mix,t=n} - [i]_f) - \rho_f([j]_{mix,t=n} - [j]_f)\rho_s([i]_{mix,t=n} - [i]_s)}{\rho_f[i]_f(\rho_s([j]_{mix,t=n} - [j]_s) - \rho_f([j]_{mix,t=n} - [j]_f))} \quad (7)$$

$$X_s = 1 - X_f - X_{wf} \quad (8)$$

The fraction of feedstock that has dissolved is calculated from the proportion of the weathered feedstock residue endmember relative to the sum of feedstock and weathered feedstock residue endmembers:

$$\tau_j = \frac{X_{wf}}{X_{wf} + X_f} \quad (9)$$

Calculating τ_j requires measuring the immobile element and base cation concentration of baseline soils, feedstock, and post-weathering soil-feedstock mix samples, as well as soil and feedstock density (i.e., the density of the ground rock powder, not the rock itself). Generally, EW deployments should assess τ_j values for all base cations to be used to estimate CDR. Because these will vary between base cations, setting the system of equations as an over-constrained system is not recommended. Some feedstocks may also contain mineral phases that are not expected to dissolve on the timeline relevant for the EW deployment, which could be taken into account by

modifying the composition of the hypothetical weathered feedstock residue endmember accordingly.

This endmember mixing approach is preferrable to quantifying feedstock dissolution exclusively from the loss of cations compared to the initial soil-feedstock mix composition (equations 1 and 2) because estimating this initial composition from post-weathering measurements without knowing the exact mixing proportions (which may vary throughout a field) is non-trivial. Instead, the endmember mixing approach quantifies the dissolution fraction while also explicitly accounting for the enrichment of immobile elements due to feedstock loss from the system. Alternatively, sampling after feedstock addition (and again after weathering has occurred) can be used to resolve issues of mixing proportions. Mobile element loss should still be calculated relative to a detrital element, even when not using the detrital element to calculate feedstock addition rates [34,35,38,40].

In addition to estimating feedstock dissolution, the framework presented here can also be used to estimate the amount of initial feedstock as well as the pre-weathering feedstock-soil mix composition from the post weathering composition as well as baseline soil and feedstock data (for detailed derivation see S1.2):

$$a = (X_f + X_{wf})\, v_{sampled\ layer}\, \rho_f \quad (10)$$

$$[j]_{mix,\,t=0} = \frac{\rho_s X_s [j]_s + \rho_f (X_f + X_{wf})[j]_f}{\rho_s X_s + \rho_f (X_f + X_{wf})} \quad (11)$$

$$[i]_{mix,t=0} = \frac{\rho_s X_s [i]_s + \rho_f (X_f + X_{wf})[i]_f}{\rho_s X_s + \rho_f (X_f + X_{wf})} \quad (12)$$

Where $v_{sample\ layer}$ is the volume of the sampled layer (per hectare if a is estimated per hectare).

Here, we supply Python code as well as an example use case. Generally, the relevant calculations are defined as functions in the Python file SOMBA.py, where the calculation of τ_j is defined in the function SOMBA_tau. The code also contains additional functions to estimate pre-weathering and post-weathering mix composition from deployment data (functions SOMBA_start and SOMBA_end; see supplement S1). In addition, SOMBA.py also contains the function

SOMBA_tau_meta, which in addition to τ_j also returns the individual endmember contributions as well as additional deployment parameters calculated from post-weathering samples as defined below. We provide two Python scripts; one that loads input data and calculates the SOMBA parameters, and a second one that demonstrates the internal consistency of the framework presented here (see also supplement S1.5 and Figure S1). We furthermore provide an Excel template that calculates the dissolution fraction based on eq. 6 –9. This template may be used as a tool to analyze initial results, but ultimately thorough statistical investigation should always be based on advanced statistical modeling.

2.2 Signal-to-noise analysis

Soils are heterogeneous both on small and large spatial scales [55–62], which may pose challenges for soil-based approaches to quantify rock powder dissolution in EW field trials [31,49,51]. To assess the efficacy of the soil-based mass balance approach to quantify rock powder dissolution outlined here against the backdrop of soil heterogeneity, we conduct a signal to noise analysis grounded in soil and basalt data for EW field trials in US agricultural lands.

2.2.1 Data constraints

To use a representative basalt composition, we calculate the mean composition (in terms of base cations and Ti) of all basalts within the US that are contained in the GEOROC database [63]. Soil element concentrations as well as representative soil heterogeneity on these parameters are based on two separate datasets. We use an existing dataset of US soils [60] to constrain the elemental composition of a large number of fields (only data classified as “Row Crops” and “Small Grains” as LandCover2 variable considered). Here, each sample is considered to represent the “true” composition of a field. The analysis uses Ca+Mg as j (basalt $[j]_f = 3.11$ mol kg^{-1}), and Ti as i (basalt $[i]_f = 0.206$ mol kg^{-1}). Because the SOMBA framework requires a clear difference in $[i]$ and $[j]$ between soils and rock powders [31], we only consider soil samples as suitable fields where both $[i]$ and $[j]$ are at least 5 times lower than US basalt ($n = 130$; Figure S2). These data are used as “true” field compositions.

To constrain variance on field-level sample compositions resulting from spatial heterogeneity, we utilize a new dataset based on high-density spatial sampling (Table 1; Figure S3). This dataset of soil heterogeneity is based on new ICP-MS soil composition measurements (residual phase after exchangeable cations were leached with 1M ammonium acetate) from 5 field sites in the US with spatial sampling frequencies ranging from 0.6 – 19.8 samples ha^{-1} (7.1 – 39.6 pooled sub samples ha^{-1}). For more information on sampling and analytical procedures, see supplement S2. We fit log-normal distributions to field data (using the Python scipy.stats module), and use fitted shape parameters representing the standard deviations (σ) of the underlying normal distribution to model in-field variance. The shape parameters corresponding to field data are shown in Figure S4, and uniform distributions between the range of observed shape parameters is used to generate synthetic σ values in Monte Carlo simulations.

2.2.2 Statistical modeling

The signal-to-noise analysis developed here predicts the efficacy of detecting feedstock dissolution based on hypothetical application amounts and dissolution fractions (τ_i) and a paired sampling approach in a series of Monte Carlo simulations based on the following logic. For each modeled τ_j value, application amount, and sampling frequency (1-20 samples ha^{-1}), we:

1. Generate the number of samples to be simulated for each field from the product of sampling frequency and a simulated field size, ranging from 10-100 ha (uniform distribution). Within the US, most farms are smaller than 72 ha, but most farmland is in farms that are larger than 2000 ha [64,65], such that the values generated here represent a conservative choice.
2. Generate a set of baseline soil samples for each field based on log-normal distributions where the variance is constrained from fits to empirical data (Figure S3, Figure S4), and the generated log-normal sample distributions scaled to ensure the expected population mean is the same as the "true" field mean (see also supplement S2.3).
3. Calculate the "true" post-weathering composition for each baseline sample, based on deployment parameters (using functions SOMBA_start and SOMBA_end)—reflecting a paired sampling approach.
4. Generate variance around "true" post-weathering compositions as in 1 assuming the same variance as for baseline samples, as well as reduced variance reflecting the expected improvement due to a paired sampling approach, implemented by reducing shape

298 parameters by 50%—while this is somewhat arbitrary, the efficacy of a paired sampling
299 approach to reduce sampling variance can be tested for any real deployment.
300 5. Randomly generate uncertainty on feedstock composition from 5–10% (uniform
301 distribution; i.e. σ values of 0.05 to 0.1 for generated log normal distributions). To reflect
302 increasing thoroughness of the sampling approach, as soil sampling frequency increases
303 from 1 to 20 samples ha^{-1} we also increase the number of total samples that the composition
304 of the feedstock endmember is calculated from (from 1 to 20 samples).
305 6. Calculate the average baseline, post-weathering soil-feedstock mix, and feedstock
306 composition based on the generated samples, each called one "realization".
307 7. For each realization we calculate the dissolution fraction (based on SOMBA_tau) and
308 calculate the absolute difference compared to the true dissolution fraction (which is
309 assumed *a priori*).
310 8. We repeat this procedure one hundred times (100 realizations) and calculate the average
311 error on τ_j over all fields and realizations. This average error represents the expected error
312 on τ_j if applying this framework based on data-constrained soil heterogeneity and
313 representative US soil composition.

3 Results and discussion

3.1 Impact of immobile element enrichment on calculated dissolution fractions

Accurately accounting for immobile element enrichment in soils due to feedstock loss from the topsoil system is essential to quantifying feedstock dissolution. Here, we demonstrate the impact of this process (see 2.1) by simulating the increase in immobile element concentrations in post-weathering soil-feedstock mixtures for three different feedstock application amounts, the whole range of dissolution fractions, as well as soils with a Ti content that is 2-10 times depleted compared to US-average basalt. As expected, the enrichment of immobile elements is highest at high dissolution fractions, τ_j, as well as at low feedstock-to-soil immobile element ratios (r_i), as shown in Figure 2a where the impact is visualized by showing the difference in post-weathering to pre-weathering soil-feedstock mix composition (Δi). At constant r_i, this effect is linear with increasing τ_j, demonstrating that it scales with the amount of feedstock volume that has been lost from the system and is replaced with soil when considering constant sampled topsoil volumes. There are also instances where this process will have a negligible (>5%) effect.

The effect also increases with increasing application amounts, because at the same dissolution fraction the volume of feedstock that is lost from topsoils increases. When r_i is defined via depletion relative to a fixed feedstock composition, Δi increases with decreasing r_i, reflecting the fact that when sampling constant soil volumes, soil that replaces lost feedstock has a higher immobile element concentration. Because r_i is defined as the ratio of feedstock to soil immobile element concentrations, lower r_i reflects higher soil concentrations of i:

$$[i]_s = \frac{[i]_f}{r_i} \quad (24)$$

Note that there is also an impact of feedstock dissolution on soil base cation concentrations beyond the pure loss of feedstock (Figure S5).

When this enrichment is not accounted for, the resulting dissolution fractions are overestimated. Here we demonstrate this effect by comparing the erroneously high τ_j* as calculated from equation 1 based on pre-weathering base cation concentrations estimated by vertically projecting post-weathering [i] concentrations onto the mixing line between soil and feedstock endmembers. The difference between the erroneous τ_j* and τ_j as calculated from the endmember approach is largest at intermediate τ_j and low r_i, where it goes up to a Δ value of 0.12 (Figure 2b). The relative effect is the highest at low τ_j and approaches 100% at low dissolution fractions and differences between soil and feedstock immobile element concentrations.

In theory, one could use an immobile element that is strongly depleted in feedstock relative to soil to calculate feedstock addition from the depletion of i in the mixed sample. However, the utility of this approach is limited as the vector caused by the enrichment of immobile elements through feedstock mass loss will align with the mixing line, making it difficult to discern significant trends (Figure S6). Hence, the framework discussed here should only be applied when immobile concentrations in feedstock are greater than those present in background soil.

In contrast, calculated τ_j may be erroneously small if immobile elements used as a proxy for feedstock addition are not truly immobile. Mobilization of "immobile" elements such as Ti and Zr has been observed for example in some extremely weathered and cation depleted soils (e.g., Melfi et al., 1996; Cornu et al., 1999; Hodson, 2002). This phenomenon would cause underestimation of the amount of initially added feedstock when immobile elements are used as a proxy for feedstock addition, resulting in estimates of base cation loss and dissolution fractions that would be biased low. While this is of less concern than potentially overestimating weathering for the purpose of verifying CDR credits, it is in the interest of practitioners to test the immobility of chosen proxy elements.

3.2 Calculated dissolution fractions outside of the mixing triangle

The framework introduced here should only be applied when the post-weathering composition of the feedstock-soil mixture falls within mass balance constraints—the mixing triangle defined by the soil, feedstock, and hypothetical weathered feedstock residue endmembers (Figure 1d). For

this to be the case, the application amount and dissolution fraction need to be large enough and the difference in soil and feedstock immobile element as well as base cation content needs to be sufficiently large [31,51] such that weathering of rock powder results in a statistically significant signal. If a significant portion of the samples in the sample-resampling approach fall outside of the mass balance constraints, it is most likely a sign that the sampling strategy was not optimized for capturing the underlying spatial variation in soil chemistry and/or that soil and feedstock compositions were too similar [31]. Given that soil sampling methods have been discussed in detail in numerous places [27,51,52], we will not belabor this point.

For the framework developed here to produce compositions outside of the endmember mixing triangle, at least one of the endmember contributions to the post-weathering sample would need to be negative. Because τ_j is computed as the contribution of the weathered feedstock residue endmember relative to the sum of the same endmember and the residual feedstock endmember contributions (equation 9), if either of these contributions is negative the denominator of this fraction can approach 0, which causes instability outside of the mixing triangle. This is demonstrated in Figure 3, where τ_j is shown as a function of [i] and [j] for two hypothetical soil and feedstock compositions. As evident from Figure 3, outside of the mixing triangle τ_j tends to increase to unrealistically large absolute values. To the left of the soil endmember (indicating a hypothetical negative amount of feedstock), reasonable but unphysical τ_j can be achieved as a result of noise. These observations suggest: (1) when applied to field settings, this framework requires thorough statistical investigation to ensure that the post-weathering composition is significantly different to pure soil and pre-weathering soil-feedstock mixtures. This requires, for example, Monte Carlo-type statistical approaches in which the uncertainty introduced by all parameters (including potential corrections for control site trends to baseline data) is fully propagated into final estimates (see also Derry et al., 2025); (2) although individual samples may fall outside of the mixing triangle as a result of soil heterogeneity even if there is a robust signal overall, because mixing compositions outside the mixing plane are unstable, τ_j should always be computed based on sample population averages rather than from the average of τ_j calculated for individual samples.

3.3 Non-self averaging behavior

The framework presented here is non-self-averaging. This means that calculating τ_j for each individual sample and then taking the average does not give the same result as calculating τ_j based on the sample population average i and j concentrations. This phenomenon is particularly acute when some samples fall outside of the mixing triangle.

We demonstrate this behavior with a simple simulation (Figure S7 & Table 2). We calculate the true pre- and post-weathering soil-feedstock mixture compositions for two hypothetical deployments (250 t ha^{-1}, τ_j of 0.5 and 50 t ha^{-1}, τ_j of 0.25) and endmember compositions (using the Python functions SOMBA_start and SOMBA_end). For the calculated post-weathering composition, we simulate a set of samples based on assumed soil heterogeneities (here implemented as normal distributions with relative standard deviations of 25% and 10%, respectively) such that these two sets correspond to exemplary low- and high-resolvability deployments. For the first deployment many samples fall outside of the mixing triangle (Figure S7c). For both populations, τ_j as calculated from the average of each individual sample τ_j is not the same τ_j calculated from the population mean i and j concentrations (Table 2), with an extreme difference for the first low-resolvability scenario. This is important to consider in statistical modelling of post-deployment data, where Monte Carlo approaches (incl. bootstrapping) should always first calculate population means based on sample chemical compositions before calculating τ_j for a specific average model composition, rather than statistically resampling from distributions of sample τ_j.

3.4 Signal-to-noise analysis

The framework presented here can only yield accurate estimates of rock powder dissolution in soils when weathering signals can be picked out against background soil heterogeneity [31,48,49,51]. Here, we assess signal-to-noise in the updated framework by estimating the average error on detected dissolution fractions practitioners would observe based on specific deployment choices and spatial sampling frequencies. This analysis is based on a novel in-field dataset of high spatial density (0.6 – 19.2 ha^{-1}; Table 1), which are used to simulate in-field heterogeneity.

The average error on detected dissolution fractions decreases with increasing sampling frequency, application amounts, and dissolution fractions (Figure 4), which is consistent with previous investigations [31,51]. Based on conservative estimates of spatial heterogeneity (Figure 4a&b); the signal-to-noise analysis suggests that when cumulative application amounts exceed 100 t ha^{-1}, expected errors are on average <15% when sampling frequencies exceed 10 samples ha^{-1}. At higher dissolution fractions (τ_j = 0.5), average errors below 10% are possible with high sample density. If paired-sampling is implemented effectively the average error decreases significantly (Figure 4c&d). While the way that the reduction in variance is implemented here is somewhat arbitrary ($\sigma/2$), we would like to stress that both variance of baseline sampling as well as of reduction of variance due to paired sampling can be constrained at a field level based on deployment data. Monte Carlo simulations should then be tailored to specific field conditions to gauge the uncertainty of detected values and applicability of SOMBA.

In the context of sampling densities, it should be noted that if the spatial distance between sub-sample cores used to pool samples is larger than the spatial wavelength of soil heterogeneity, required high sample frequencies can also partially be achieved by pooling samples, as is commonly practiced in most agronomic soil sampling protocols [69]. Additionally, there are well established methods for characterizing contaminants in soils and other particulate media [70–75]. A key aspect of these methodologies, such as Incremental Sampling Methods (ISMs), is that they acknowledge a-priori that soil components are distributed unevenly at the scales of interest relevant to signal detection. When implemented properly, incremental sample pooling and averaging strategies result in highly representative soil data at the field scale [70–75], with high numbers of pooled sub-samples of sufficient individual mass having a higher utility compared to more measured samples reflecting less pooled cores, not least because the former tend to be normally distributed due to the central limit theorem. We assert that if the mean and variance of a field or fields can be well established, averaged mixing models such as SOMBA can be utilized with confidence commensurate to the established population statistics.

This analysis is based on a subset of samples for which SOMBA are suitable for MRV, here operationally defined as soil [i] and [j] being at least 5 times below US-average basalt composition [63]. Approximately ~22% of all agricultural soils contained in the used geochemical soil database

464 ^{60} fulfill this condition. This fraction strongly increases when all soils with concentrations at least
465 2 times lower are considered (n = 594 out of 614 samples; ~95%), primarily due to more samples
466 fulfilling the Ti cutoff (Figure S8). When the same signal-to-noise analysis is applied to this larger
467 set of fields the average error on detected mass transfer coefficients is larger (Figure S9). This is
468 expected based on lower soil-feedstock compositional differences [31]. Note also that the modeled
469 deployment size (10-100 ha) has a direct impact on the signal-to-noise analysis as the number of
470 generated samples is the product between field/deployment size and sampling frequency.
471
472 In addition to increasing application amounts and optimizing deployment parameters e.g., through
473 the choice of an above-average Ti containing basalt [31], improving sampling protocols [51] can all
474 help to improve the robustness of SOMBA. An alternative way to increase both accuracy and
475 precision could be to quantify dissolution fractions at the aggregate level over multiple
476 deployments rather than for individual field sites, as has for example been demonstrated for the
477 quantification of changes in soil organic carbon stocks [20,76].
478
479 Our signal-to-noise analysis also demonstrates that SOMBA can produce robust estimates of rock
480 powder dissolution under specific conditions. Nevertheless, resolvability also depends on the
481 practice decisions with respect to acceptable uncertainty. While achieving an error of less than,
482 e.g., 10% for 90% of the realizations [51] is challenging in most settings unless application rates are
483 high, larger uncertainties can still be acceptable in the context of crediting CDR if crediting is done
484 at lower bounds of uncertainty [27]. In addition, it is important to keep in mind that this approach
485 requires an adequate difference in soil and feedstock composition. A signal-to-noise analysis for a
486 given feedstock should hence only be based on the subset of soils that are potential targets for
487 robust signals for this MRV approach, rather than through approaches that group all signals
488 together regardless of soil fitness. Furthermore, it is important to note that what is relevant for this
489 framework is the total application *amount*, not the annual *rate*. Hence, settings for which feedstock
490 dissolution may not be resolvable initially can become resolvable over time through the gradual
491 increase of cumulative application amounts as well as increases in the dissolution fraction over
492 time.
493

3.5 Additional Assumptions and Limitations

One key assumption that is made in the signal-to-noise analysis is that baseline soil [*i*] and [*j*] does not change with time, and that therefore as long as sampling and spatial heterogeneity is correctly accounted for, a change in [*i*] and [*j*] can be solely attributed to feedstock addition and dissolution. This assumption may not always hold in cases where weathering of a labile constituent of the soil, aeolian deposition, or other process might unexpectedly result in loss or gain of elements in the soil. Changes through time in soil [*i*] and [*j*] in controls that cannot be explained by sampling practice and spatial heterogeneity should be factored into estimates for feedstock weathering generated using SOMBA; and results treated with caution where a mechanistic understanding of the elemental concentration change of the system cannot be found.

We have not included baseline trend corrections in the signal-to-noise analysis presented here due to a lack of data on covariance for temporal trends in adjacent fields. Any simulation would hence depend more on our assumptions than realistic processes. As has been demonstrated, e.g., for soil organic carbon monitoring [76], including such a correction would increase average detection errors but not systematically change trends relating to different application amounts and sampling protocols. Importantly, we suggest that for the purpose of crediting, cation losses from control sites should be deducted from treatment site EW signals, but that control site gains in base cations must not be used to increase weathering signals from treatment sites unless the cation gain in control site composition can be explained by known manipulations that has also occurred on treatment sites (e.g., fertilizer input etc.).

4 Implications

We have presented an updated framework for using SOMBA to quantify rock powder dissolution in EW field settings and provide Python code for implementing this framework. The updated framework explicitly accounts for the enrichment of immobile elements in topsoils due to feedstock mass loss [34,40]. Failing to account for these processes can cause detected dissolution fractions to be up to ~0.12 too high. Depending on deployment parameters, this may be an error of up to 100%.

We strongly suggest that the framework presented here should only be used when post-weathering sample compositions fall robustly within the mass balance constraints defined by the endmember mixing approach. Solutions are unstable outside of this parameter space, which may yield dissolution fractions that are unphysically high or low and should not be used to estimate CDR. The code presented here generates sensible dissolution fractions when the post-weathering composition falls within the mass balance dictated mixing triangle. However, this does not necessarily mean that this signal can be resolved statistically. It is the responsibility of practitioners to thoroughly investigate the statistical significance of changes in soil compositions and deduced rock dissolution parameters, for example through stochastic simulations that propagate uncertainties pertaining to all relevant parameters (Derry et al., 2025), including resulting from trends in control sites and through downsampling statistical tests. Sampling protocols should generally be defined *a priori* informed by desired sampling power [77]. Lastly, we suggest that the framework should always be applied to calculate dissolution fractions based on the sample population mean, rather than for each individual sample. This consideration will change the statistical modelling of weathering dynamics, e.g. via Monte Carlo simulations. Future studies should include incremental sampling strategies at predefined field and sub-field scales. In effect, averaging strategies should be fit-for-purpose and built in concert with the soil sampling procedures that researchers or EW suppliers design. We would also like to stress that alternative parametrizations of SOMBA are feasible and may be advantageous for certain settings such that the framework presented here should not be viewed as un-amendable.

Our signal-to-noise analysis suggests that field-level quantification of rock powder dissolution based on SOMBA is possible when application amounts, dissolution fractions, soil-feedstock compositional differences, and sampling frequencies are sufficient. This may for example imply that signal emergence will only become resolvable after multiple years of repeated deployments and after substantial feedstock weathering. Our analysis suggests that SOMBA can be a useful tool in tracking weathering rates, but it must be acknowledged that this approach will not work in all settings and will typically require higher sampling densities than those currently being implemented in commercial deployments. Signal emergence can furthermore be optimized using tailored sampling strategies [51] as well as feedstock-soil-matching [31].

5 Acknowledgements

TJS acknowledges funding by the Swiss National Science Foundation (Grant P500PN_210790). NP and CR acknowledge funding from the United States Department of Agriculture (USDA) and the Grantham Foundation for the Environment. TS and NP acknowledge support from the Yale Center for Natural Carbon Capture. SL and SZ acknowledge support from College of Arts & Sciences Environment and Sustainability Initiative (ESI) at Texas A&M University.

6 Conflict of interest

JJ is funded through the public benefit corporation, Mati Carbon, a subsidiary of the not-for profit-Swaniti Initiative.

The remaining authors declare that the research was conducted in the absence of any commercial or financial relationships that could be construed as a potential conflict of interest.

7 Bibliography

(1) IPCC. Global Warming of 1.5°C. An IPCC Special Report on the Impacts of Global Warming of 1.5°C above Pre-Industrial Levels and Related Global Greenhouse Gas Emission Pathways, in the Context of Strengthening the Global Response to the Threat of Climate Change,. *Ipcc - Sr15* **2018**, *2* (October), 17–20.

(2) Geden, O.; Gidden, M. J.; Lamb, W. F.; Minx, J. C.; Nemet, G. F.; Smith, S. M. The State of Carbon Dioxide Removal. **2024**.

(3) UNEP. *Emissions Gap Report 2024: No More Hot Air … Please! With a Massive Gap between Rhetoric and Reality, Countries Draft New Climate Commitments*; United Nations Environment Program, Nairobi, Kenya, 2024. https://doi.org/10.59117/20.500.11822/46404 This.

(4) Seifritz, W. CO2 Disposal by Means of Silicates. *Nature* **1990**, *345* (June), 486.

(5) Schuiling, R. D.; Krijgsman, P. Enhanced Weathering: An Effective and Cheap Tool to Sequester CO2. *Clim Change* **2006**, *74* (1–3), 349–354. https://doi.org/10.1007/s10584-005-3485-y.

(6) Hartmann, J.; Kempe, S. What Is the Maximum Potential for CO2 Sequestration by "Stimulated" Weathering on the Global Scale? *Naturwissenschaften* **2008**, *95* (12), 1159–1164. https://doi.org/10.1007/s00114-008-0434-4.

(7) Köhler, P.; Hartmann, J.; Wolf-Gladrow, D. A. Geoengineering Potential of Artificially Enhanced Silicate Weathering of Olivine. *Proc Natl Acad Sci U S A* **2010**, *107* (47), 20228–20233. https://doi.org/10.1073/pnas.1000545107.

(8) ten Berge, H. F. M.; van der Meer, H. G.; Steenhuizen, J. W.; Goedhart, P. W.; Knops, P.; Verhagen, J. Olivine Weathering in Soil, and Its Effects on Growth and Nutrient Uptake in Ryegrass (Lolium Perenne L.): A Pot Experiment. *PLoS One* **2012**, *7* (8), 1–8. https://doi.org/10.1371/journal.pone.0042098.

(9) Hartmann, J.; West, A. J.; Renforth, P.; Köhler, P.; De La Rocha, C. L.; Wolf-Gladrow, D. A.; Dürr, H. H.; Scheffran, J. Enhanced Chemical Weathering as a Geoengineering Strategy to Reduce Atmospheric Carbon Dioxide, Supply Nutrients, and Mitigate Ocean Acidification. *Reviews of Geophysics* **2013**, *51* (2), 113–149. https://doi.org/10.1002/rog.20004.

(10) Beerling, D. J.; Leake, J. R.; Long, S. P.; Scholes, J. D.; Ton, J.; Nelson, P. N.; Bird, M.; Kantzas, E.; Taylor, L. L.; Sarkar, B.; Kelland, M.; Delucia, E.; Kantola, I.; Müller, C.; Rau, G. H.; Hansen, J. Farming with Crops and Rocks to Address Global Climate, Food and Soil Security. *Nat Plants* **2018**, *4* (March). https://doi.org/10.1038/s41477-018-0108-y.

(11) Beerling, D. J.; Kantzas, E. P.; Lomas, M. R.; Wade, P.; Eufrasio, R. M.; Renforth, P.; Sarkar, B.; Andrews, M. G.; James, R. H.; Pearce, C. R.; Mercure, J.; Pollitt, H.; Holden, P. B.; Edwards, N. R. Potential for Large-Scale CO2 Removal via Enhanced Rock Weathering with Croplands. *Nature* **2020**, *583* (May 2018), 242–248. https://doi.org/10.1038/s41586-020-2448-9.

(12) Beerling, D. J.; Epihov, D. Z.; Kantola, I. B.; Masters, M. D.; Reershemius, T.; Planavsky, N. J.; Reinhard, C. T.; Jordan, J. S.; Thorne, S. J.; Weber, J.; Martin, M. V.; Freckleton, R. P.; Hartley, S. E.; James, R. H.; Pearce, C. R.; DeLucia, E. H.; Banwart, S. A. Enhanced Weathering in the US Corn Belt Delivers Carbon Removal with Agronomic Benefits.

Proceedings of the National Academy of Sciences **2024**, *120*, 2017. https://doi.org/10.1073/pnas.2319436121.

(13) Renforth, P.; Henderson, G. Assessing Ocean Alkalinity for Carbon Sequestration. *Reviews of Geophysics* **2017**, *55* (3), 636–674. https://doi.org/10.1002/2016RG000533.

(14) Gunnarsen, K. C.; Jensen, L. S.; Rosing, M. T.; Dietzen, C. Greenlandic Glacial Rock Flour Improves Crop Yield in Organic Agricultural Production. *Nutr Cycl Agroecosyst* **2023**, *126* (1), 51–66. https://doi.org/10.1007/s10705-023-10274-0.

(15) Haque, F.; Santos, R. M.; Chiang, Y. W. Optimizing Inorganic Carbon Sequestration and Crop Yield With Wollastonite Soil Amendment in a Microplot Study. *Front Plant Sci* **2020**, *11* (July), 1–12. https://doi.org/10.3389/fpls.2020.01012.

(16) Kelland, M. E.; Wade, P. W.; Lewis, A. L.; Taylor, L. L.; Sarkar, B.; Andrews, M. G.; Lomas, M. R.; Cotton, T. E. A.; Kemp, S. J.; James, R. H.; Pearce, C. R.; Hartley, S. E.; Hodson, M. E.; Leake, J. R.; Banwart, S. A.; Beerling, D. J. Increased Yield and CO2 Sequestration Potential with the C4 Cereal Sorghum Bicolor Cultivated in Basaltic Rock Dust-Amended Agricultural Soil. *Glob Chang Biol* **2020**, *26* (6), 3658–3676. https://doi.org/10.1111/gcb.15089.

(17) Smith, S. M.; Geden, O.; Affairs, S.; Minx, J. C.; Change, C. The State of Carbon Dioxide Removal. **2023**.

(18) CDR.fyi. *Keep Calm and Remove On - The CDR Fyi 2024 Year in Review*; 2025.

(19) Parton, W. J.; Hartman, M.; Ojima, D.; Schimel, D. Daycent Description and Testing. **1998**, 35–48.

(20) Potash, E.; Bradford, M. A.; Oldfield, E. E.; Guan, K. Measure-and-Remeasure as an Economically Feasible Approach to Crediting Soil Organic Carbon at Scale. *Environmental Research Letters* **2025**, *20* (2). https://doi.org/10.1088/1748-9326/ada16c.

(21) Oldfield, B. E. E.; Eagle, A. J.; Rubin, R. L.; Rudek, J.; Gordon, D. R. Crediting Agricultural Soil Carbon Sequestration; Regional Consistency Is Necessary for Carbon Credit Integrity. *Science (1979)* **2022**, *375* (6586), 1222–1225.

(22) Kanzaki, Y.; Chiaravalloti, I.; Zhang, S.; Planavsky, N. J.; Reinhard, C. T. In Silico Calculation of Soil PH by SCEPTER v1.0. *Geosci Model Dev* **2024**, *17* (10), 4515–4532. https://doi.org/10.5194/gmd-17-4515-2024.

(23) Kanzaki, Y.; Zhang, S.; Planavsky, N. J.; Reinhard, C. T. Soil Cycles of Elements Simulator for Predicting TERrestrial Regulation of Greenhouse Gases: SCEPTER v0.9. *Geosci Model Dev* **2022**, *15* (12), 4959–4990. https://doi.org/10.5194/gmd-15-4959-2022.

(24) Bertagni, M. B.; Calabrese, S.; Cipolla, G.; Valerio Noto, L.; Porporato, A. M. Advancing Enhanced Weathering Modeling in Soils: Systematic Comparison and Validation with Experimental Data. *J Adv Model Earth Syst* **2024**, 1–25. https://doi.org/10.1029/2024MS004224.

(25) Taylor, L. L.; Beerling, D. J.; Quegan, S.; Banwart, S. A. Simulating Carbon Capture by Enhanced Weathering with Croplands: An Overview of Key Processes Highlighting Areas of Future Model Development. *Biol Lett* **2017**, *13* (4). https://doi.org/10.1098/rsbl.2016.0868.

(26) Kanzaki, Y.; Planavsky, N.; Zhang, S.; Jordan, J.; Suhrhoff, T. J.; Christopher, T. Soil Cation Storage Is a Key Control on the Carbon Removal Dynamics of Enhanced Weathering. *Environmental Research Letters* **2025**, *20*, 1–11. https://doi.org/10.1088/1748-9326/ade0d5.

(27) Sutherland, K.; Holme, E.; Savage, R.; Gill, S.; Matlin-Wainer, M.; He, J.; Marsland, E.; Patel, C. Isometric Enhanced Weathering in Agriculture v1.0. Isometric 2024. https://registry.isometric.com/protocol/enhanced-weathering-agriculture.

(28) Clarkson, M. O.; Larkin, C. S.; Swoboda, P.; Reershemius, T.; Suhrhoff, T. J.; Maesano, C. N.; Campbell, J. S. A Review of Measurement for Quantification of Carbon Dioxide Removal by Enhanced Weathering in Soil. *Frontiers in Climate* **2024**, *6* (June), 1–20. https://doi.org/10.3389/fclim.2024.1345224.

(29) Almaraz, M.; Bingham, N. L.; Holzer, I. O.; Geoghegan, E. K.; Goertzen, H.; Sohng, J.; Houlton, B. Z. Methods for Determining the CO2 Removal Capacity of Enhanced Weathering in Agronomic Settings. *Frontiers in Climate* **2022**, *4*. https://doi.org/10.3389/fclim.2022.970429.

(30) Reershemius, T.; Kelland, M. E.; Davis, I. R.; D'Ascanio, R.; Kalderon-Asael, B.; Asael, D.; Suhrhoff, T. J.; Epihov, D. E.; Beerling, D. J.; Reinhard, C. T.; Planavsky, N. J. Initial Validation of a Soil-Based Mass-Balance Approach for Empirical Monitoring of Enhanced Rock Weathering Rates. *Environ Sci Technol* **2023**, *57* (48), 19497–19507. https://doi.org/10.1021/acs.est.3c03609.

(31) Suhrhoff, T. J.; Reershemius, T.; Wang, J.; Jordan, J. S.; Reinhard, C. T.; Planavsky, N. J. A Tool for Assessing the Sensitivity of Soil-Based Approaches for Quantifying Enhanced Weathering: A US Case Study. *Frontiers in Climate* **2024**, *6* (1346117), 1–17. https://doi.org/10.3389/fclim.2024.1346117.

(32) te Pas, E. E. E. M.; Chang, E.; Marklein, A. R.; Comans, R. N. J.; Hagens, M. Accounting for Retarded Weathering Products in Comparing Methods for Quantifying Carbon Dioxide Removal in a Short-Term Enhanced Weathering Study. *Frontiers in Climate* **2025**, *1524998* (February), 1–10. https://doi.org/10.3389/fclim.2024.1524998.

(33) Dietzen, C.; Rosing, M. T. Quantification of CO2 Uptake by Enhanced Weathering of Silicate Minerals Applied to Acidic Soils. *International Journal of Greenhouse Gas Control* **2023**, *125* (March), 103872. https://doi.org/10.1016/j.ijggc.2023.103872.

(34) Brimhall, G. H.; Dietrich, W. E. Constitutive Mass Balance Relations between Chemical Composition, Volume, Density, Porosity, and Strain in Metasomatic Hydrochemical Systems: Results on Weathering and Pedogenesis. *Geochemica et Cosmochemica Acta* **1987**, *51* (4). https://doi.org/10.1016/0016-7037(87)90070-6.

(35) Chadwick, O. A.; Brimhall, G. H.; Hendricks, D. M. From a Black to a Gray Box - a Mass Balance Interpretation of Pedogenesis. *Geomorphology* **1990**, *3* (3–4), 369–390. https://doi.org/10.1016/0169-555X(90)90012-F.

(36) Kurtz, A. C.; Derry, L. A.; Chadwick, O. A.; Alfano, M. J. Refractory Element Mobility in Volcanic Soils. *Geology* **2000**, *28* (8), 683–686. https://doi.org/10.1130/0091-7613(2000)028<0683:REMIVS>2.3.CO;2.

(37) Chadwick, O. A.; Derry, L. A.; Vitousek, P. M.; Huebert, B. J.; Hedin, L. O. Changing Sources of Nutrients during Four Million Years of Ecosystem Development. *Nature* **1999**, *397* (6719), 491–497. https://doi.org/10.1038/17276.

(38) Brimhall, G. H.; Christopher J., L.; Ford, C.; Bratt, J.; Taylor, G.; Warin, O. Quantitative Geochemical Approach to Pedogenesis: Importance of Parent Material Reduction, Volumetric Expansion, and Eolian Influx in Lateritization. *Geoderma* **1991**, *51* (1–4), 51–91. https://doi.org/10.1016/0016-7061(91)90066-3.

(39) White, A. F.; Bullen, T. D.; Schulz, M. S.; Blum, A. E.; Huntington, T. G.; Peters, N. E. Differential Rates of Feldspar Weathering in Granitic Regoliths. *Geochim Cosmochim Acta* **2001**, *65* (6), 847–869. https://doi.org/10.1016/S0016-7037(00)00577-9.

(40) Anderson, S. P.; Dietrich, W. E.; Brimhall, G. H. Weathering Profiles, Mass-Balance Analysis, and Rates of Solute Loss: Linkages between Weathering and Erosion in a Small, Steep Catchment. *Bulletin of the Geological Society of America* **2002**, *114* (9), 1143–1158. https://doi.org/10.1130/0016-7606(2002)114<1143:WPMBAA>2.0.CO.

(41) Riebe, C. S.; Kirchner, J. W.; Finkel, R. C. Long-Term Rates of Chemical Weathering and Physical Erosion from Cosmogenic Nuclides and Geochemical Mass Balance. *Geochim Cosmochim Acta* **2003**, *67* (22), 4411–4427. https://doi.org/10.1016/S0016-7037(03)00382-X.

(42) Tabor, N. J.; Montanez, I. P.; Zierenberg, R.; Currie, B. S. Mineralogical and Geochemical Evolution of a Basalt-Hosted Fossil Soil (Late Triassic, Ischigualasto Formation, Northwest Argentina): Potential for Paleoenvironmental Reconstruction. *Bulletin of the Geological Society of America* **2004**, *116* (9–10), 1280–1293. https://doi.org/10.1130/B25222.1.

(43) Sheldon, N. D.; Tabor, N. J. Quantitative Paleoenvironmental and Paleoclimatic Reconstruction Using Paleosols. *Earth Sci Rev* **2009**, *95* (1–2), 1–52. https://doi.org/10.1016/j.earscirev.2009.03.004.

(44) Brantley, S. L.; Lebedeva, M. Learning to Read the Chemistry of Regolith to Understand the Critical Zone. *Annu Rev Earth Planet Sci* **2011**, *39*, 387–416. https://doi.org/10.1146/annurev-earth-040809-152321.

(45) Fisher, B. A.; Rendahl, A. K.; Aufdenkampe, A. K.; Yoo, K. Quantifying Weathering on Variable Rocks, an Extension of Geochemical Mass Balance: Critical Zone and Landscape Evolution. *Earth Surf Process Landf* **2017**, *42* (14), 2457–2468. https://doi.org/10.1002/esp.4212.

(46) Lipp, A. G.; Shorttle, O.; Sperling, E. A.; Brocks, J. J.; Cole, D. B.; Crockford, P. W.; Del Mouro, L.; Dewing, K.; Dornbos, S. Q.; Emmings, J. F.; Farrell, U. C.; Jarrett, A.; Johnson, B. W.; Kabanov, P.; Keller, C. B.; Kunzmann, M.; Miller, A. J.; Mills, N. T.; O'Connell, B.; Peters, S. E.; Planavsky, N. J.; Ritzer, S. R.; Schoepfer, S. D.; Wilby, P. R.; Yang, J. The Composition and Weathering of the Continents over Geologic Time. *Geochem Perspect Lett* **2021**, *17*, 21–26. https://doi.org/10.7185/geochemlet.2109.

(47) Kantola, I. B.; Blanc-Betes, E.; Master, M. D.; Chang, E.; Marklein, A.; Moore, C. E.; von Haden, A.; Bernacchi, C. J.; Wolf, A.; Epihov, D. Z.; Beerling, D. J.; Delucia, E. H. Improved Net Carbon Budgets in the US Midwest through Direct Measured Impacts of Enhanced Weathering. *Glob Chang Biol* **2023**, No. May, 1–17. https://doi.org/10.1111/gcb.16903.

(48) Reershemius, T.; Suhrhoff, T. J. On Error, Uncertainty, and Assumptions in Calculating Carbon Dioxide Removal Rates by Enhanced Rock Weathering in Kantola et al ., 2023. *Glob Chang Biol* **2023**, No. October, 1–3. https://doi.org/10.1111/gcb.17025.

(49) Derry, L. A.; Chadwick, O. A.; Porder, S. Estimation of Carbon Dioxide Removal via Enhanced Weathering. *Glob Chang Biol* **2025**, *31*, 1–3. https://doi.org/10.1111/gcb.70067.

(50) Baum, M.; Liu, H.; Schacht, L.; Schneider, J.; Yap, M. *Mass-Balance MRV for Carbon Dioxide Removal by Enhanced Rock Weathering: Methods, Simulation, and Inference*; 2024. https://doi.org/10.48550/arXiv.2407.01949.

(51) Rogers, B.; Maher, K. A Framework for Integrating Spatial Uncertainty into Critical Zone Models : Application to Enhanced Weathering. *CDRXIV* **2025**. https://doi.org/10.70212/cdrxiv.2025334.v1.
(52) Campbell, J.; Bastianini, L.; Buckman, J.; Bullock, L.; Foteinis, S.; Furey, V.; Hamilton, J.; Harrington, K.; Hawrot, O.; Holdship, P.; Knapp, W.; Maesano, C.; Mayes, W.; Pogge von Strandmann, P.; Reershemius, T.; Rosair, G.; Sturgeon, F.; Turvey, C.; Wilson, S.; Renforth, P. *Measurements in Geochemical Carbon Dioxide Removal*, 1st ed.; Heriot-Watt University, 2023. https://doi.org/10.17861/2GE7-RE08.
(53) Zhang, S.; Reinhard, C. T.; Liu, S.; Kanzaki, Y.; Noah, J. Constraining Carbon Loss from Rivers Following Terrestrial Enhanced Rock Weathering. *ESS Open Archive* **2024**. https://doi.org/10.22541/essoar.171052489.97497425/v1.
(54) Kanzaki, Y.; Planavsky, N. J.; Reinhard, C. T. New Estimates of the Storage Permanence and Ocean Co-Benefits of Enhanced Rock Weathering. *PNAS Nexus* **2023**, *2* (4), 1–9. https://doi.org/10.1093/pnasnexus/pgad059.
(55) Webster, R.; Lark, R. M. Analysis of Variance in Soil Research: Examining the Assumptions. *Eur J Soil Sci* **2019**, *70* (5), 990–1000. https://doi.org/10.1111/ejss.12804.
(56) Ramsey, M. H.; Solomon-Wisdom, G.; Argyraki, A. Evaluation of in Situ Heterogeneity of Elements in Solids: Implications for Analytical Geochemistry. *Geostand Geoanal Res* **2013**, *37* (4), 379–391. https://doi.org/10.1111/j.1751-908X.2013.00236.x.
(57) McGrath, D.; Zhang, C.; Carton, O. T. Geostatistical Analyses and Hazard Assessment on Soil Lead in Silvermines Area, Ireland. *Environmental Pollution* **2004**, *127* (2), 239–248. https://doi.org/10.1016/j.envpol.2003.07.002.
(58) Jackson, R. B.; Caldwell, M. M. Geostatistical Patterns of Soil Heterogeneity Around Individual Perennial Plants. *J Ecol* **1993**, *81* (4), 683. https://doi.org/10.2307/2261666.
(59) Zhang, C.; Selinus, O.; Schedin, J. Statistical Analyses for Heavy Metal Contents in till and Root Samples in an Area of Southeastern Sweden. *Science of the Total Environment* **1998**, *212* (2–3), 217–232. https://doi.org/10.1016/S0048-9697(97)00341-0.
(60) Smith, D. B.; Cannon, W. F.; Woodruff, L. G.; Solano, F.; Kilburn, J. E.; Fey, D. L. Geochemical and Mineralogical Data for Soils of the Conterminous United States. *U.S. Geological Survey Data Series* **2013**, *801* (April), 1–26. https://doi.org/10.3133/ds801.
(61) Bahri, A.; Berndtsson, R.; Jinno, K. Spatial Dependence of Geochemical Elements in a Semiarid Agricultural Field: I. Scale Properties. *Soil Science Society of America Journal* **1993**, *57* (5), 1316–1322. https://doi.org/10.2136/sssaj1993.03615995005700050026x.
(62) Spijker, J.; Vriend, S. P.; Van Gaans, P. F. M. Natural and Anthropogenic Patterns of Covariance and Spatial Variability of Minor and Trace Elements in Agricultural Topsoil. *Geoderma* **2005**, *127* (1–2), 24–35. https://doi.org/10.1016/j.geoderma.2004.11.002.
(63) Lehnert, K.; Su, Y.; Langmuir, C. H.; Sarbas, B.; Nohl, U. A Global Geochemical Database Structure for Rocks. *Geochemistry, Geophysics, Geosystems* **2000**, *1* (5). https://doi.org/10.1029/1999gc000026.
(64) USDA. Farms and Farmland. *2022 Census of Agriculture Highlights*. U.S. Department of Agriculture, National Agricultural Statistics Service 2024.
(65) USDA. Farms and Land in Farms 2021 Summary. *United States Department of Agriculture: National Agricultural Statistics Service* **2022**, No. February, 1995–2004.
(66) Cornu, S.; Lucas, Y.; Lebon, E.; Ambrosi, J. P.; Luizão, F.; Rouiller, J.; Bonnay, M.; Neal, C. Evidence of Titanium Mobility in Soil Profiles, Manaus, Central Amazonia. *Geoderma* **1999**, *91* (3–4), 281–295. https://doi.org/10.1016/S0016-7061(99)00007-5.

(67) Hodson, M. E. Experimental Evidence for Mobility of Zr and Other Trace Elements in Soils. *Geochim Cosmochim Acta* **2002**, *66* (5), 819–828. https://doi.org/10.1016/S0016-7037(01)00803-1.
(68) Melfi, A. J.; Subies, F.; Nahon, D.; Formoso, M. L. L. Zirconium Mobility in Bauxites of Southern Brazil. *J South Am Earth Sci* **1996**, *9* (3–4), 161–170. https://doi.org/10.1016/0895-9811(96)00003-x.
(69) Sawyer, J.; Mallarino, A.; Killorn, R. *Take a Good Soil Sample to Help Make Good Fertilization Decisions*; 2016.
(70) Clausen, J. L.; Georgian, T.; Bednar, A. *Cost and Performance Report of Incremental Sampling Methodology for Soil Containing Metallic Residues Engineer Research and Development Center*; 2013.
(71) Hewitt, A. D.; Jenkins, T. F.; Walsh, M. E.; Walsh, M. R.; Bigl, S. R.; Ramsey, C. A. *Protocols for Collection of Surface Soil Samples at Military Training and Testing Ranges for the Characterization of Energetic Munitions Constituents*; 2007.
(72) Clausen, J. L.; Georgnian, T.; Bednar, A.; Perron, N.; Bray, A.; Tuminello, P.; Gooch, G.; Mulherin, N.; Gelvin, A.; Beede, M.; Saari, S.; Jones, W.; Tazik, S. *Demonstration of Incremental Sampling Methodology for Soil Containing Metallic Residues*; 2013.
(73) Clausen, J.; Gerogian, T.; Bednar, A. *Incremental Sampling Methodology (ISM) for Metallic Residues*; 2013.
(74) Hadley, P. W.; Crapps, E.; Hewitt, A. D. Time for a Change of Scene. *Environ Forensics* **2011**, *12* (4), 312–318. https://doi.org/10.1080/15275922.2011.622344.
(75) ITRC. *Incremental Sampling Methodology (ISM) Update The Interstate Technology & Regulatory Council (ITRC)*; 2020.
(76) Bradford, M. A.; Eash, L.; Polussa, A.; Jevon, F. V.; Kuebbing, S. E.; Hammac, W. A.; Rosenzweig, S.; Oldfield, E. E. Testing the Feasibility of Quantifying Change in Agricultural Soil Carbon Stocks through Empirical Sampling. *Geoderma* **2023**, *440* (July), 116719. https://doi.org/10.1016/j.geoderma.2023.116719.
(77) Chow, S. C.; Cheng, B.; Cosmatos, D. On Power and Sample Size Calculation for QT Studies with Recording Replicates at given Time Point. *J Biopharm Stat* **2008**, *18* (3), 483–493. https://doi.org/10.1080/10543400801995452.
(78) Potapov, P.; Turubanova, S.; Hansen, M. C.; Tyukavina, A.; Zalles, V.; Khan, A.; Song, X. P.; Pickens, A.; Shen, Q.; Cortez, J. Global Maps of Cropland Extent and Change Show Accelerated Cropland Expansion in the Twenty-First Century. *Nat Food* **2022**, *3* (1), 19–28. https://doi.org/10.1038/s43016-021-00429-z.

8 Figures

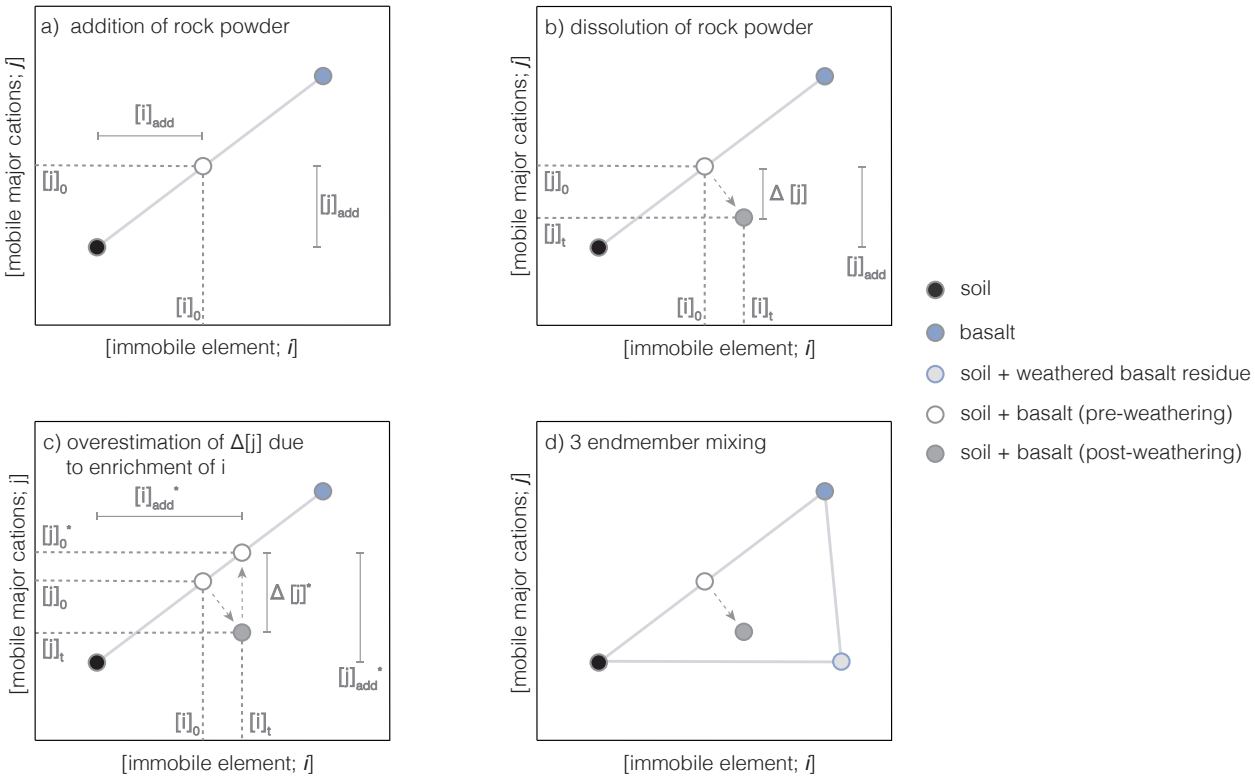

Figure 1: Sketch of the soil-based mass balance framework to quantify rock powder dissolution in soils. After rock powder of an elevated base cation and immobile element concentration compared to baseline soils is added to a field, the composition of the initial soil-feedstock mix falls on the mixing line between both endmembers (a). As feedstock dissolves base cations are released and either stored on the soil exchange complex or flushed out of topsoils. At the same time immobile element concentrations increase as a result of feedstock mass and volume loss, resulting in a vector starting at the pre-weathering soil-feedstock mix composition towards the bottom right (b). This is important to take into account, because simply projecting the post-weathering soil-feedstock mix composition from its immobile element concentration up to the mixing line between soil and feedstock endmembers will cause inflated estimates of cation mass loss and deduced dissolution fractions (c). One way to estimate the dissolution fraction while taking into account the impact of feedstock mass loss is to use a three endmember mixing model where the post-weathering composition is described as a mix of the baseline soil, pure feedstock, and a hypothetical weathered feedstock residue endmember (d). Note that the offset in immobile element concentrations (i.e., enrichment of immobile element concentrations due to mass loss) for the post-weathering soil-feedstock mix sample is exaggerated in panels b-d for the purpose of visualization. In a realistic system the horizontal component of this vector would be smaller compared to the vector between basalt as well as soil + weathered basalt residue (proportionally to the position of the pre-weathering soil-feedstock mix composition on the missing line).

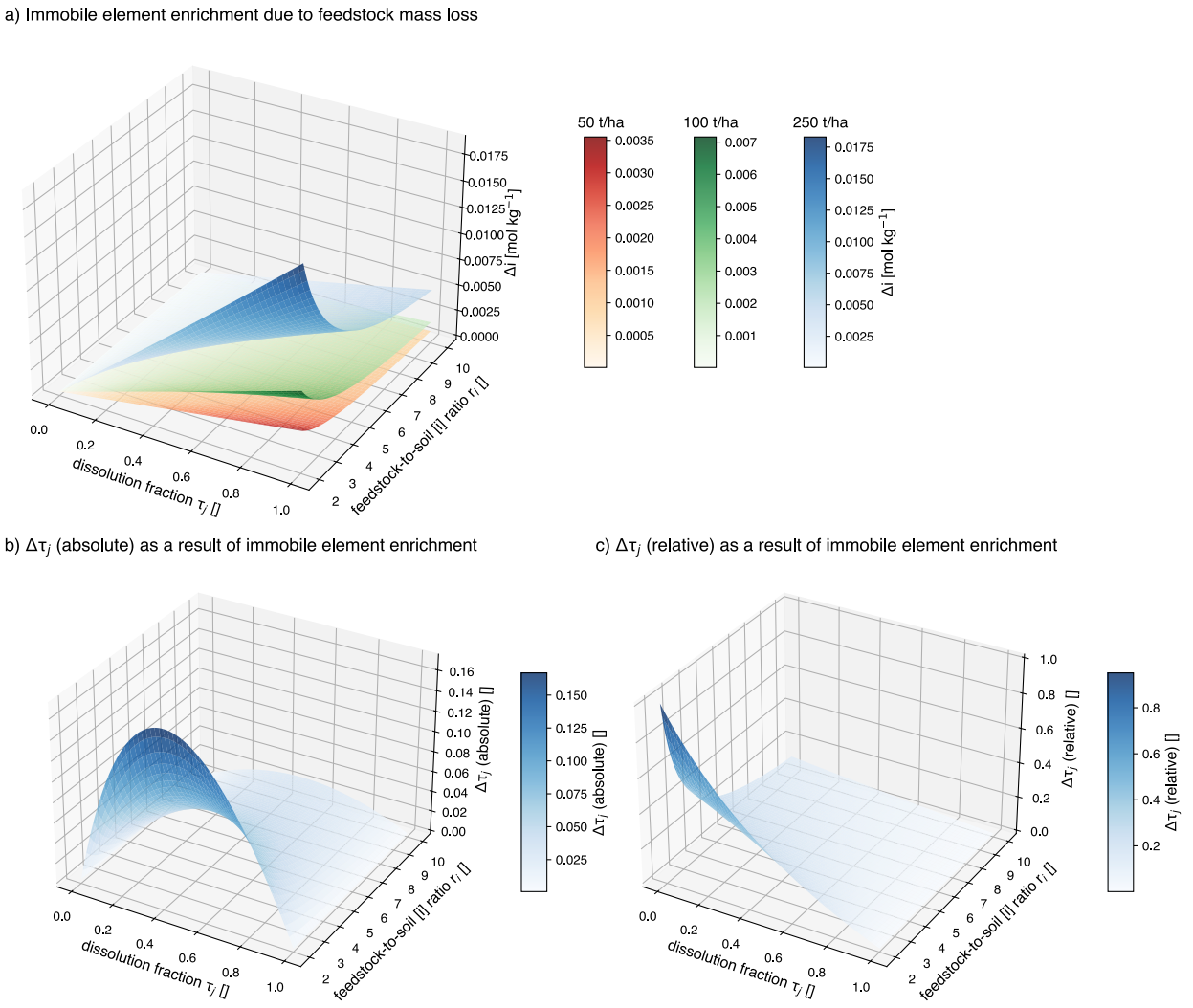

Figure 2: The dissolution of added rock powder increases the immobile element concentration of topsoils of constant volume as the lost rock powder is replaced by soil from the bottom of the soil column (a). The difference between erroneously high τ_j when not taking this process into account and the actual τ_j is shown in b for absolute values (τ_j* - τ_j) and in c relative to the respective τ_j. ((τ_j* - τ_j) / τ_j).*

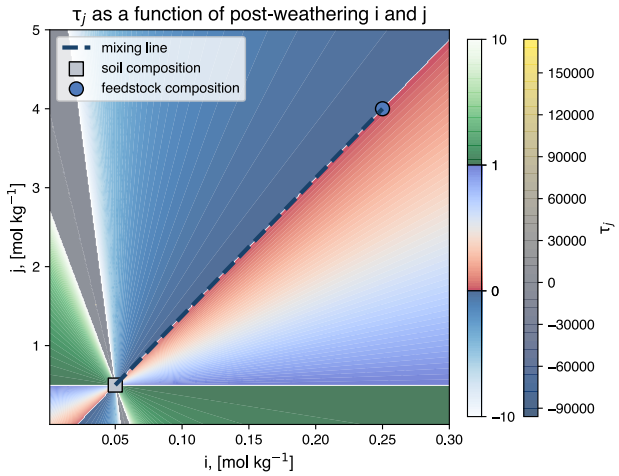

Figure 3: Quantified feedstock dissolution fractions (τ_j) for a hypothetical soil and rock powder for a range of immobile element (i) and base cation (j) concentrations. The framework developed here should only be applied within the mixing triangle set out by baseline soil, rock powder, and the hypothetical weathered feedstock residue endmember. Outside of this domain, the results of the framework are unstable, and absolute values can approach infinity because negative contributions of endmembers can cause the dominator of equation 9 to approach 0. Generally, the framework developed here should only be applied when post-weathering soil-feedstock mix composition robustly falls within the mixing triangle.

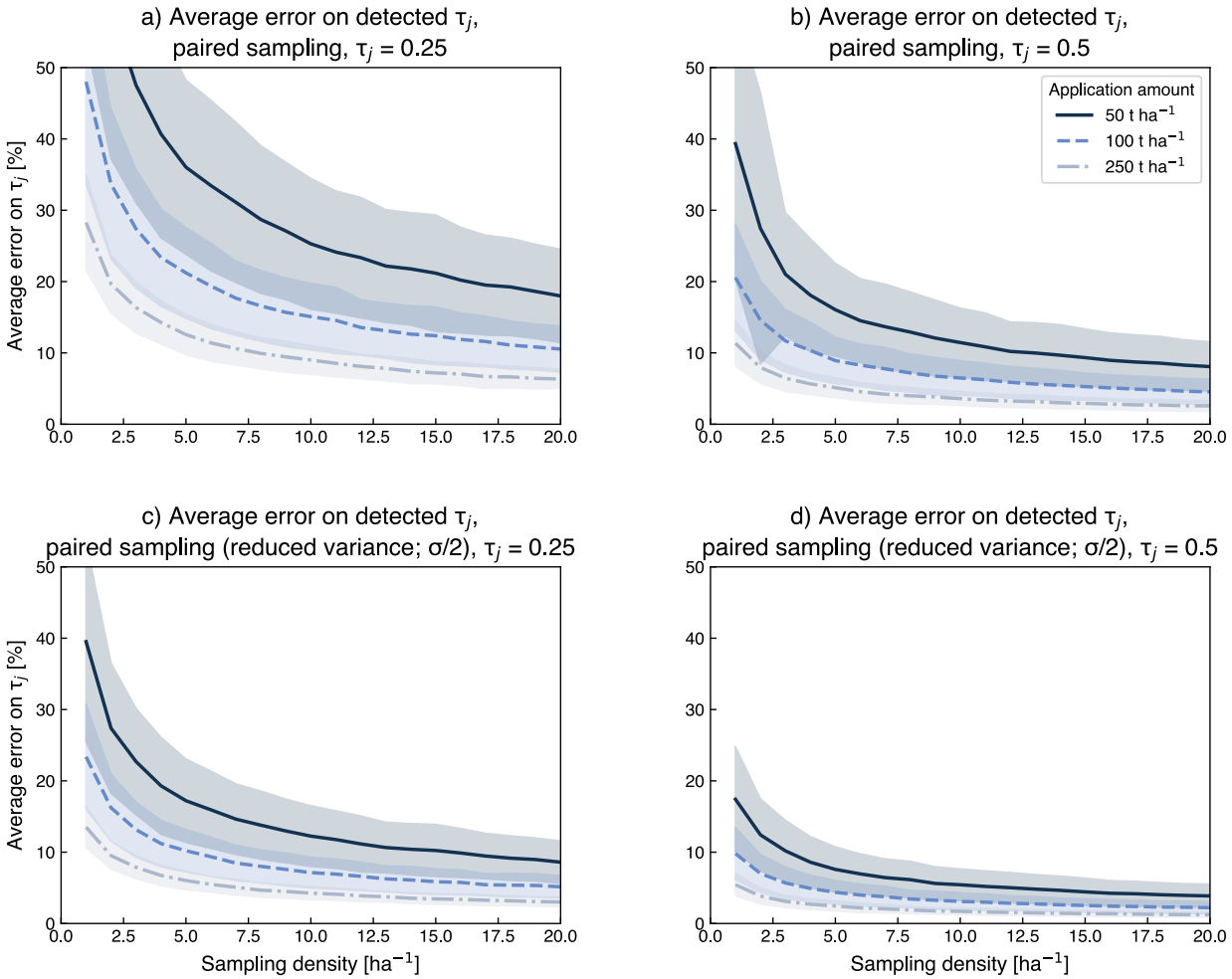

Figure 4: Average errors on detected dissolution fractions for two simulated mass transfer coefficients (τ_j = 0.25 in a and c, τ_j = 0.5 in b and d). The top row shows simulations where the variance imposed onto paired samples is equivalent to the variance of initial baseline samples. Because is likely an overestimate for accurate sample and resample strategies, the lower row shows the same simulations based on reduced variance for resampled sample composition (σ/2). The simulations are based on compositions of US soil [60] and basalt [63] considering soils with base cation and Ti concentrations at least 5 times lower than basalt. The simulated in-field soil heterogeneity is based on the novel field trial dataset presented in Table 1.

9 Tables

Table 1: Information on the field sites used to constrain spatial heterogeneity in the signal-to-noise analysis. The number of pooled cores corresponds to the number of-sub sample cores that were combined for each measured sample. Soil heterogeneity refers to the σ of log-normal fits to soil concentration distributions normalized to the field mean such that the resulting distribution has a mean of 1 (Figure S3). Site names are anonymized and location data are rounded to one decimal degree to protect farmer privacy.

								soil heterogeneity (σ; log-normal)			
Site name	**Lat**	**Lon**	**size**	**# samples**	**# pooled cores**	**sample density**	**core density**	**Ca**	**Mg**	**Na**	**Ti**
	[°]	[°]	[ha]			[ha^{-1}]	[ha^{-1}]	[]	[]	[]	[]
Site 1	45.3	-87.6	6.42	40	2	6.23	12.46	0.493	0.278	0.072	0.120
Site 2	42.3	-73.6	5.08	41	2	8.07	16.14	0.395	0.309	0.250	0.288
Site 3	31.3	-84.4	2.02	40	2	19.80	39.60	0.582	0.218	0.630	0.264
Site 4	35.8	-78.2	42.44	25	12	0.59	7.07	0.519	0.523	0.510	0.154
Site 5	35.8	-78.2	26.85	38	12	1.42	16.98	0.355	0.687	0.391	0.177

872 *Table 2: Realized sample compositions and their calculated τ_j as well as population average sample composition and its τ_j for two*
873 *hypothetical EW deployments (50 t ha^{-1}, τ_j = 0.25, SD of randomly generated soil compositions = 25% as well as 250 t ha^{-1}, τ_j =*
874 *0.5, 1SD = 10%).*

example deployment 1 50 t ha^{-1}, τ_j = 0.25, SD = 0.25			**example deployment 2 250 t ha^{-1}, τ_j = 0.5, SD = 0.1**		
i [mol kg^{-1}]	j [mol kg^{-1}]	τ_j []	i [mol kg^{-1}]	j [mol kg^{-1}]	τ_j []
I. random samples (post-deployment composition)					
0.033	0.569	1.300	0.089	0.707	0.652
0.054	0.777	-1.525	0.082	0.808	0.400
0.053	0.389	8.379	0.093	0.698	0.694
0.076	0.522	0.940	0.085	0.764	0.515
0.078	0.365	1.374	0.096	0.924	0.413
0.035	0.723	2.392	0.096	0.893	0.452
0.061	0.564	0.631	0.072	0.846	0.078
0.051	0.455	6.083	0.079	0.880	0.217
0.063	0.641	0.313	0.096	0.751	0.635
0.066	0.623	0.506	0.093	0.817	0.519
random sample average τ_j		2.039			0.457
II. sample average [i], [j], and related τ_j					
0.057	0.563	0.433	0.088	0.809	0.481
III. calculated true composition					
0.057	0.591	0.25	0.089	0.802	0.5

875

Supplementary information to

Updated framework and signal-to-noise analysis of soil mass balance approaches for quantifying enhanced weathering on managed lands

Tim Jesper Suhrhoff[1,2 *], Tom Reershemius[3, 2], Jacob Jordan[4], Shihan Li[5], Shuang Zhang[5], Ella Milliken[2], Boriana Kalderon-Asael[2], Christopher T. Reinhard[6], Noah J. Planavsky[2,1]

[1] Yale Center for Natural Carbon Capture, Yale University, New Haven, CT 06511, USA
[2] Department of Earth and Planetary Sciences, Yale University, New Haven, CT 06511, USA
[3] School of Natural and Environmental Sciences, Newcastle University, Newcastle upon Tyne, England NE1 7RU, United Kingdom
[4] Mati Carbon, Houston, TX, USA
[5] Department of Oceanography, Texas A&M University, College Station, TX 77843, USA
[6] School of Earth & Atmospheric Sciences, Georgia Institute of Technology, Atlanta, GA 30332, USA

* corresponding author: timjesper.suhrhoff@yale.edu

Python code and Excel templates for the soil mass balance framework can be found here:

Content of this file:

S1 Additional derivations of the soil mass balance framework

This supplement contains all derivations relating to section 2.1 of the manuscript. In addition to quantifying rock powder dissolution and deployment parameters based on post-weathering soil sample composition (see section 2.1 of the main text), we also present a framework to calculate expected pre- and post-weathering compositions for soil-feedstock mixtures. The associated Python functions are included in the Python file SOMBA.py and were used in the analyses presented here. The code can be assessed here:
https://doi.org/10.5281/zenodo.15696933

S1.1 Derivation of soil mass balance framework

We continue from section 2.1 after the introduction of the hypothetical weathered feedstock endmember. The composition of this hypothetical endmember is defined to be the composition that a layer of soil would have after a layer of pure feedstock (corresponding to the soil sampling depth, d_{sample}) has dissolved.

Since cations are assumed to be lost from the system, it has the same cation content as an equivalent layer of pure soil, i.e.:

$$[j]_{wf} = [j]_s \quad \text{S1}$$

where the subscripts *wf* and *s* correspond to weathered feedstock residue and baseline soil (and *f* denotes pure feedstock in the following equations). The immobile element concentration of this endmember is given by summing the amount of immobile elements in the fully weathered feedstock as well as the soil that has replaced the feedstock in the reference volume, and dividing by the system mass after weathering (assumed to be the same as background soil mass/density for the equivalent soil volume):

$$[i]_{wf} = \frac{\rho_s v_{sampled\ layer}\,[i]_s + \rho_f v_{sampled\ layer}[i]_f}{\rho_s v_{sampled\ layer}} = \frac{\rho_s[i]_s + \rho_f[i]_f}{\rho_s} = [i]_s + {}^{\rho_f}/_{\rho_s}\,[i]_f \quad \text{S2}$$

where $v_{sampled\ layer}$ corresponds to the sampled soil volume and ρ to the density of feedstock and soil. We make the assumption that post-weathering density is equivalent to background soil density (see also eq. S6b) within the frame of reference assuming no change in porosity, though we note that this ignores weathering congruency and compositional difference between the soil parent material and the rock feedstock applied.

Assuming mass and volume conservation, this endmember mixing approach can be described by a system of equations such that each endmember contributes a volume proportion (X) to the observed post-weathering composition, which together sum to unity:

$$X_s + X_f + X_{wf} = 1 \quad \text{S3}$$

Because in practical field sampling based on constant soil sampling depths, a system of constant *volume* is sampled, these endmember contributions reflect *volume* contributions to the sampled soil volume defined by the sampling depth over a given area (all calculations and code shared here use 1 hectare (ha) by default). The endmember contributions reflect three unknowns. Hence, we set up two additional equations reflecting mass conservation of immobile elements as well as mobile base cations respectively.

$$[j]_s X_s \rho_s + [j]_f X_f \rho_f + [j]_{wf} X_{wf} \rho_{wf} = [j]_{mix,t=n}(X_s \rho_s + X_f \rho_f + X_{wf} \rho_{wf}) \quad \text{S4}$$

$$[i]_s X_s \rho_s + [i]_f X_f \rho_f + [i]_{wf} X_{wf} \rho_{wf} = [i]_{mix,t=n}(X_s \rho_s + X_f \rho_f + X_{wf} \rho_{wf}) \quad \text{S5}$$

Assuming that:

$$[j]_{wf} = [j]_s \ , and \quad \text{S6a}$$

$$\rho_{wf} = \rho_s \quad \text{S6b}$$

gives:

$$[j]_s X_s \rho_s + [j]_f X_f \rho_f + [j]_s X_{wf} \rho_s = [j]_{mix,t=n}(X_s \rho_s + X_f \rho_f + X_{wf} \rho_s) \quad \text{S7}$$

$$[i]_s X_s \rho_s + [i]_f X_f \rho_f + [i]_{wf} X_{wf} \rho_s = [i]_{mix,t=n}(X_s \rho_s + X_f \rho_f + X_{wf} \rho_s) \quad \text{S8}$$

Now, rearranging eq. S7 and S8 to isolate the endmember contributions on one side of the equation:

$$X_s \rho_s([j]_{mix,t=n} - [j]_s) + X_f \rho_f([j]_{mix,t=n} - [j]_f) + X_{wf} \rho_s([j]_{mix,t=n} - [j]_s) = 0 \quad \text{S9}$$

$$X_s \rho_s([i]_{mix,t=n} - [i]_s) + X_f \rho_f([i]_{mix,t=n} - [i]_f) + X_{wf} \rho_s([i]_{mix,t=n} - [i]_{wf}) = 0 \quad \text{S10}$$

Next, we substitute $[i]_{wf}$ from eq. S2 into S10:

$$X_s \rho_s([i]_{mix,t=n} - [i]_s) + X_f \rho_f([i]_{mix,t=n} - [i]_f) + X_{wf} \rho_s \left([i]_{mix,t=n} - [i]_s - {}^{\rho_f}/_{\rho_s}[i]_f\right) = 0 \quad \text{S11}$$

For clarity, we rewrite the system of equations (S3, S7, S8) in matrix form:

$$\begin{pmatrix} \rho_s([j]_{mix,t=n} - [j]_s) & \rho_f([j]_{mix,t=n} - [j]_f) & \rho_s([j]_{mix,t=n} - [j]_s) \\ \rho_s([i]_{mix,t=n} - [i]_s) & \rho_f([i]_{mix,t=n} - [i]_f) & \rho_s\left([i]_{mix,t=n} - [i]_s - {}^{\rho_f}/_{\rho_s}[i]_f\right) \\ 1 & 1 & 1 \end{pmatrix} * \begin{pmatrix} X_s \\ X_f \\ X_{wf} \end{pmatrix} = \begin{pmatrix} 0 \\ 0 \\ 1 \end{pmatrix} \quad \text{S12}$$

For clarity, defining the following shorthand notions:

$$a = \rho_s([j]_{mix,t=n} - [j]_s) \quad \text{S13a}$$

$$b = \rho_f([j]_{mix,t=n} - [j]_f) \quad \text{S13b}$$

$$c = \rho_s([i]_{mix,t=n} - [i]_s) \quad \text{S13c}$$

$$d = \rho_f([i]_{mix,t=n} - [i]_f) \quad \text{S13d}$$

$$e = \rho_f[i]_f \quad \text{S13e}$$

With these shorthand notations, equation S12 becomes:

$$\begin{pmatrix} a & b & a \\ c & d & c - e \\ 1 & 1 & 1 \end{pmatrix} * \begin{pmatrix} X_s \\ X_f \\ X_{wf} \end{pmatrix} = \begin{pmatrix} 0 \\ 0 \\ 1 \end{pmatrix} \quad \text{S14}$$

Now defining a new variable reflecting the sum of the soil and weathered feedstock residue endmembers:

$$X_s' = X_s + X_{wf} \quad \text{S15}$$

Inserting S15 into S14, the system of equations reduces to:

$$aX_s' + bX_f = 0 \quad \text{S16}$$

$$cX_s' + dX_f - eX_{wf} = 0 \quad \text{S17}$$

$$X_s' + X_f = 1 \quad \text{S18}$$

Now we solve for X_s' by substituting $X_f = 1 - X_s'$ from equation S18 into S16:

$$aX_s' + b(1 - X_s') = 0 \quad \text{S19a}$$

$$aX_s' + b - bX_s' = 0 \quad \text{S19b}$$

$$(a - b)X_s' + b = 0 \quad \text{S19c}$$

$$X_s' = \frac{-b}{a-b} \quad \text{S19d}$$

Now, substituting, S19d into $X_f = 1 - X_s'$ from equation S18:

$$X_f = 1 - \frac{-b}{a-b} = \frac{a-b}{a-b} - \frac{-b}{a-b} = \frac{a-b+b}{a-b} = \frac{a}{a-b} \quad \text{S20}$$

Substituting S13a and S13b into S20:

$$X_f = \frac{\rho_s([j]_{mix,t=n} - [j]_s)}{\left(\rho_s([j]_{mix,t=n} - [j]_s) - \rho_f([j]_{mix,t=n} - [j]_f)\right)} \quad \text{S21}$$

Now we substitute S20 and S19d into S17 to solve for X_{wf}:

$$c\frac{-b}{a-b} + d\frac{a}{a-b} - eX_{wf} = 0 \quad \text{S22}$$

$$\frac{-bc+ad}{a-b} - eX_{wf} = 0 \quad \text{S23}$$

$$X_{wf} = \frac{ad-bc}{e(a-b)} \quad \text{S24}$$

Finally, substituting S13a-S13e into S24:

$$X_{wf} = \frac{\rho_s([j]_{mix,t=n}-[j]_s)\rho_f([i]_{mix,t=n}-[i]_f)-\rho_f([j]_{mix,t=n}-[j]_f)\rho_s([i]_{mix,t=n}-[i]_s)}{\rho_f[i]_f(\rho_s([j]_{mix,t=n}-[j]_s)-\rho_f([j]_{mix,t=n}-[j]_f))} \quad \text{S25}$$

S1.2 Calculation of deployment parameters from post-weathering samples

From the estimates of endmember contributions to the post-weathering soil-feedstock mix sample as well as the rock powder dissolution calculated using the approach outlined above, additional deployment parameters can be calculated that may be valuable for the purposes of MRV. First, we can calculate the mass of rock powder initially added to the sampled soil volume (a, t ha^{-1}):

$$a = fV_{f,t=0}\, v_{sampled\ layer}\, \rho_f \quad \text{S26}$$

where $fV_{f,t=0}$ is the pre-weathering feedstock volume fraction, defined as the sum of the volume fraction comprising residual feedstock as well as the initial feedstock present that has since weathered:

$$fV_{f,t=0} = X_f + X_{wf} \quad \text{S27}$$

and the sampled layer volume per hectare is calculated from the sampling depth ($d_{sampling}$):

$$v_{sampled\ layer}[m^3\ ha^{-1}] = 10000\ m^2 ha^{-1} * d_{sampling}[m] \quad \text{S28}$$

Note that in cases where the sampling depth is not the same as the soil mixing depth, it is important to use the depth of soil sampling. If the two depths are not the same, using calculated parameters

that are based only on the sampled layer for the entire mixed layer assumes that the sampled layer composition is representative of the entire mixed layer. This is not necessarily the case, particularly when feedstock distribution is not uniform with depth. In cases where the mixing depth is larger than the sampling depth, one could assume that the calculated dissolution fraction (τ_j) applies to the known application amount, but this would trade off against the benefit that feedstock addition can be calculated from the enrichment of immobile elements. To make sure that the calculation of initial CDR from a combination of τ_j with the applied feedstock mass is entirely constrained in empirical measurements the choice of sampling depth should ideally be equal to the mixing depth.

In addition, we can calculate the initial soil-feedstock mix composition from the post-weathering composition and mixing model outputs. Initial concentrations can be calculated by combining the amounts of base cations as well as immobile elements contributed to the initial mix from both soil and feedstock divided by the mass of the system:

$$[j]_{mix,\ t=0} = \frac{\rho_s\, v_{s,t=0}\, [j]_s + \rho_f\, v_{f,t=0}\, [j]_f}{\rho_s\, v_{s,t=0} + \rho_f\, v_{f,t=0}} \quad \text{S30}$$

$$[i]_{mix,\ t=0} = \frac{\rho_s\, v_{s,t=0} [i]_s + \rho_f\, v_{f,t=0}\, [i]_f}{\rho_s\, v_{s,t=0} + \rho_f\, v_{f,t=0}} \quad \text{S31}$$

where $v_{s,t=0}$ and $v_{f,t=0}$ are the area normalized volumes ($m^3\ ha^{-1}$) of soil and feedstock within the sampled topsoil volume:

$$v_{s,t=0} = v_{sampled\ layer}\, X_s \quad \text{S32}$$

$$v_{f,t=0} = v_{sampled\ layer}\, fV_{f,t=0} = v_{sampled\ layer}(X_f + X_{wf}) \quad \text{S33}$$

Substituting 20 and 21 in 18 and 19:

$$[j]_{mix,\ t=0} = \frac{\rho_s\, v_{sampled\ layer}\, X_s\, [j]_s + \rho_f\, v_{sampled\ layer}(X_f + X_{wf})[j]_f}{\rho_s\, v_{sampled\ layer}\, X_s + \rho_f\, v_{sampled\ layer}(X_f + X_{wf})} = \frac{\rho_s\, X_s\, [j]_s + \rho_f(X_f + X_{wf})[j]_f}{\rho_s\, X_s + \rho_f(X_f + X_{wf})} \quad \text{S34}$$

$$[i]_{mix,t=0} = \frac{\rho_s v_{sampled\ layer}\, X_s\, [i]_s + \rho_f\, v_{sampled\ layer}(X_f + X_{wf})[i]_f}{\rho_s\, v_{sampled\ layer}\, X_s + \rho_f v_{sampled\ layer}(X_f + X_{wf})} = \frac{\rho_s\, X_s\, [i]_s + \rho_f(X_f + X_{wf})[i]_f}{\rho_s\, X_s + \rho_f(X_f + X_{wf})} \quad \text{S35}$$

The calculation of feedstock application mass as well as pre-weathering composition from post-weathering composition and deployment data is included in the SOMBA_TAU_meta function defined in the SOMBA.py file in the supplement.

S1.3 Pre-weathering mix composition

After addition of rock powder to soils, the composition of the soil-rock-powder mix falls on a mixing line between both endmembers (Figure 1a). Provided the rock powder is enriched in both base cations as well as at least one immobile element compared to the baseline soil, the addition of rock powder causes an increase of both base cation and immobile element concentrations. The pre-weathering mix concentrations of both major cations (j) and an immobile element (i; both in mol/kg) can be calculated from the mix of both endmembers:

$$j_{mix,t=0} = j_f \, r_{m,t=0} + j_s \, (1 - fM_{f,t=0}) \quad \text{S36}$$

$$i_{mix,t=0} = i_f \, r_{m,t=0} + i_s \, (1 - fM_{f,t=0}) \quad \text{S37}$$

Where the subscripts *f* and *s* denote feedstock and soil respectively, and fM_f refers to the mass mixing ratio of feedstock in the soil-feedstock mix, which can be calculated as:

$$fM_{f,t=0} = \frac{a}{(a + m_{soil,t=0})} \quad \text{S38}$$

where *a* is the application amount of rock powder (in t ha^{-1}), and $m_{topsoil,t=0}$ is the mass of soil in the mixed soil rock powder topsoil layer right after deployment (in t ha^{-1}). The application amount *a* is in this case given from deployment data, while the mass of topsoil can be calculated from the topsoil volume that is not rock powder (units in square brackets):

$$m_{soil,t=0}\,[t\,ha^{-1}] = v_{soil,t=0}[m^3 ha^{-1}]\,\rho_{soil}[t\,m^{-3}] \quad \text{S39}$$

$$v_{soil,t=0}[m^3 ha^{-1}] = v_{mixed\ layer}[m^3 ha^{-1}] - v_f[m^3 ha^{-1}] \quad \text{S40}$$

$$v_{f,t=0}[m^3 ha^{-1}] = \frac{a\,[t\,ha^{-1}]}{\rho_f\,[t\,m^3]} \quad \text{S41}$$

$$v_{mixed\ layer}[m^3 ha^{-1}] = 10000\ [m^2 ha^{-1}]\ d_{mix}\ [m] \quad \text{S42}$$

where m refers to mass, v to volume, and ρ to density of the soil within the mixed layer (subscript topsoil), the total mixed layer (mixed layer) as defined by the mixing depth (d_{mix}), as well as the feedstock (f). Substituting S39-42 into S38:

$$fM_{f,t=0} = \frac{a}{(a+(10000\ d_{mix} - {}^{a}/_{\rho_f})\ \rho_{soil})} \quad \text{S43}$$

S1.4 Post-weathering composition

As feedstock dissolves, both base cation as well as immobile element concentrations change. While base cation concentrations decrease as these mobile elements are leached from topsoils, immobile element concentrations increase due to the loss of feedstock mass (and volume) from topsoils, resulting in a vector originating at the pre-weathering composition towards the bottom right in j vs. i space (Figure 1a). The post-weathering soil-rock powder mix composition can be calculated as a function of feedstock dissolution (mass transfer coefficient τ_j) fraction through system mass conservation where the denominate describes the mass of the post-weathering mix and the numerator its amount base cations or immobile elements:

$$j_{mix,t=n} = \frac{\rho_s v_{s,t=n}[j]_s + \rho_f v_{f,t=n}[j]_f}{\rho_s v_{s,t=n} + \rho_f v_{f,t=n}} \quad \text{S44}$$

$$i_{mix,t=n} = \frac{\rho_s v_{s,t=n}[i]_s + \rho_f v_{f,t=0}[i]_f}{\rho_s v_{s,t=n} + \rho_f v_{f,t=n}} \quad \text{S45}$$

where the $t = 0$ in the numerator of eq. S45 reflects the fact that immobile elements added through feedstock are retained within topsoils upon weathering. Post-weathering soil and feedstock volumes can be calculated as:

$$v_{f,t=n} = v_{f,t=0}\ (1 - \tau_j) \quad \text{S46}$$

$$v_{s,t=n} = v_{f,t=0} + v_{f,t=0} - v_{f,t=n} = v_{s,t=0} + v_{f,t=0}\ \tau_j \quad \text{S47}$$

S1.5 Internal consistency of the SOMBA framework

One of the script contained in the code supplement (SOMBA_verification.py) demonstrates the internal consistency of the SOMBA framework. In the first part of the script, an example dataset is generated based on assumed deployment parameters. Some of these parameters—such as the amount of feedstock applied, the dissolution fraction, and others—are specifically required for the SOMBA_start and SOMBA_end functions. These functions estimate the composition of the soil-feedstock mix before and after weathering, respectively, using deployment-specific inputs. However, when using the soil mass balance framework to estimate rock powder dissolution fractions from post-weathering samples, these parameters may not be necessary.

In the second part of the script, the generated dataset is used to sequentially call a series of soil mass balance functions defined in the SOMBA.py file, which are derived here. The functions called include: (1) SOMBA_start, which calculates the pre-weathering soil-feedstock mix composition from deployment parameters; (2) SOMBA_end, which estimates the post-weathering composition based on the output from SOMBA_start and an assumed rock powder dissolution fraction; (3) SOMBA_tau, which calculates the rock powder dissolution fraction from deployment data, including baseline soil, feedstock, and post-weathering compositions; and (4) SOMBA_tau_meta, which performs the same calculation as SOMBA_tau but also provides metadata such as endmember contributions and detected feedstock amounts.

Finally, the exported Figure S1 demonstrates that the calculated from the SOMBA framework (such as τ_j and pre-weathering concentrations) are equivalent to the values assumed or calculated *a-priori*. The same is true for the estimate rock powder application amount—in this case it is important to consider potential mismatches between mixing and sampling depth, where the detected rock powder amount is going to be less than the amount assumed *a-priori* if the sampling depth is less than the mixing depth.

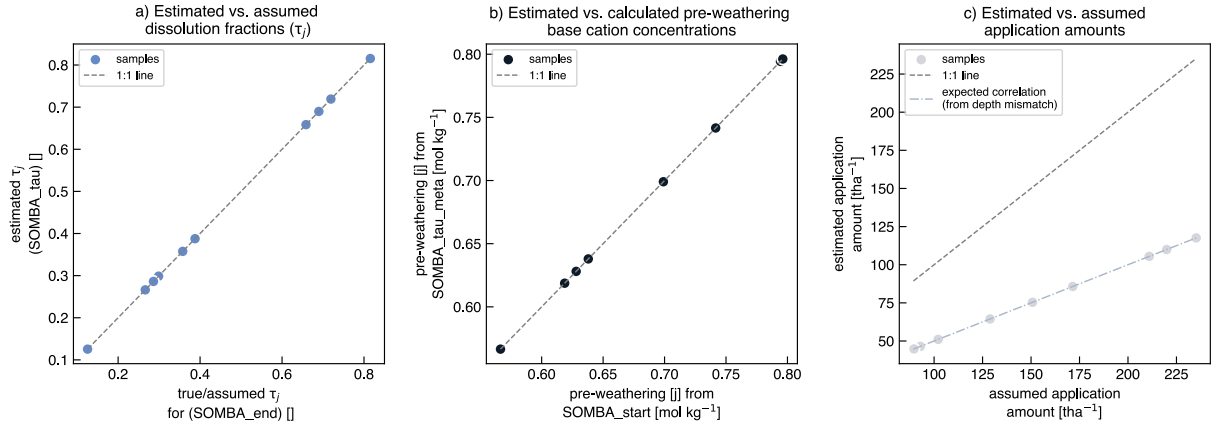

Figure S1: This figure demonstrates that the soil mass balance framework developed here is internally consistent. The calculated dissolution fraction τ_j (a) and pre-weathering soil concentration (b) are equivalent to the values assumed a-priori. The same is true for detected rock powder application amounts (c) when taking into account potential mismatches between soil mixing and sampling depth.

S2 Soil data

S2.1 Site and sampling information

Site 1: This field is classified as loamy-sand, with a mean pH of 7.0, and is on a corn-yellow pea rotation. The only fertilizer used is chicken litter.

Site 2: This field is classified as silt-loam, with a mean pH of 6.4. This field is used as pastureland, growing native grasses for grazing. There is no tillage, irrigation, fertilizer, or liming use.

Site 3: This field is classified as loamy-sand. This field is used for peanuts, and is irrigated by a center pivot. There is no tillage, regular nitrogen application, and highly infrequent liming.

Site 4 and 5: Both fields are managed by the same farmer. The fields are no-till and are ripped every 3 years. Both fields are on a corn-soy rotation, and receive nitrogen fertilizer during corn season. There is no irrigation. No pH data is available for this field.

The first 3 sites were sampled in a grid array across the entire field region, with 2 cores taken at each sampling location and homogenized. Samples were dried at 60 °C, sieved to 2mm and ground prior to analysis. Site 4 and 5 samples were collected by randomly pooling 12 15-cm drill cores from a 1m radius circle. Samples were dried at 60 °C, sieved to 2mm and ground prior to analysis.

The locations of the field sites as well as of the soil samples used to constrain field composition are shown in Figure S2 below.

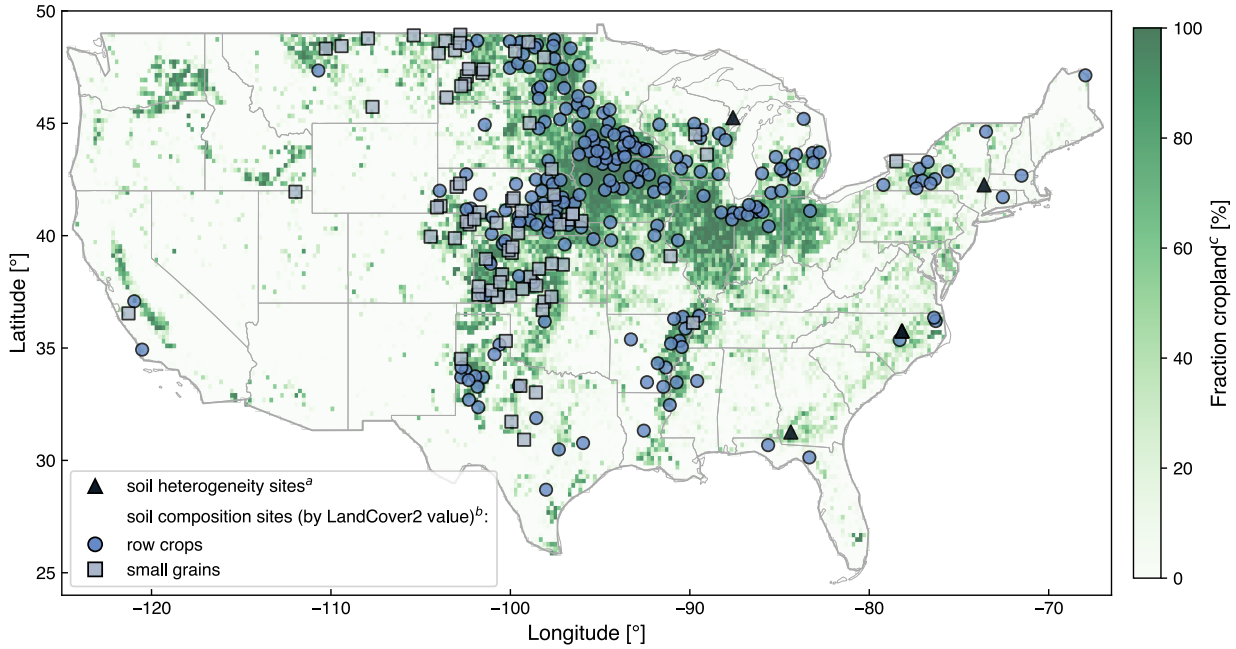

Figure S2: Sites of the data utilized to constrain soil composition as well as in-field spatial heterogeneity (Table 1).
[a] Novel soil heterogeneity dataset reported here.
[b] 60
[c] 78

S2.2 Analytical information

Powdered soil samples (typically 0.1 g) were leached in 12 ml of 1M Ammonium Acetate (trace metal grade) and centrifuged in 15 ml polypropylene tubes for 5 minutes at 4000 rpm to release any adsorbed cations (i.e, the exchangeable fraction) and subsequently washed in 2 ml of 2X MilliQ H_2O (18.2MΩcm at 25 °C) and centrifuged again. The soil was then transferred into pre-acid-cleaned quartz crucibles, dried at 60 °C and ashed at 600 °C to incinerate any organic matter (and release volatiles). The dried residue was weighed for insoluble content and to estimate the LOI. The residue was then transferred into pre-acid-cleaned teflon beakers and dissolved completely using a mixture of 5 ml distilled hydrochloric acid (HCl), 5 ml distilled nitric acid (HNO3) and 1 ml of trace metal grade hydrofluoric acid (HF), capped, heated at 100 °C for 24 hours. The samples were then uncapped and evaporated to dryness at 90 °C and redissolved in 5 ml of 6N HCl.

Splits were taken for elemental concentrations measurements. For analysis on the Agilent 8900 Triple Quadrupole ICP-MS, a split of 15 µl from each sample was evaporated, diluted 1000 times with 1% HNO3 (v/v) and spiked with ^{26}Mg and ^{49}Ti. Indium was introduced externally as an internal standard. For analysis on the Thermo Scientific Element XR ICP-MS, a split of 10 µl from each sample was evaporated, diluted 400 times with 5% HNO3 (v/v) and spiked with ^{26}Mg, ^{42}Ca, ^{49}Ti and 1ppb In. Values were normalized using routine measurements of USGS geostandards BHVO-2 and SGR-1b (processed with each batch of samples throughout the entire procedure), whose precision was within 1% of certified values (4% for Al) on the Agilent (LL). For more information on the analytical procedure see also Reershemius et al. (2023).

S2.3 Implementation of soil heterogeneity in Monte Carlo simulations

We use soil composition data from five novel field sites sampled at high spatial densities to constrain in-field heterogeneity for the Monte Carlo signal-to-noise analysis. The data are normalized by the field mean concentration (Figure S3) before we fit log-normal distributions to make sure the population means are 1. The use of log-normal (rather than normal) distributions is intentional because samples generated from log-normal distributions always have positive values, preventing the occurrence of non-physical negative soil concentrations in the signal-to-noise analysis without having to filter some data. For normal distributions, this could be achieved by simply filtering out negative model occurrences, but this would change the mean of generated sample distributions and cause a systematic error in calculated dissolution fractions. In addition, using log-normal compared to normal fits also represents a conservative choice for the signal-to-noise analysis due to the generally higher variance, as well has overall better fits compared to normal distributions (R^2 better for 11 out of 20 elemental field distributions).

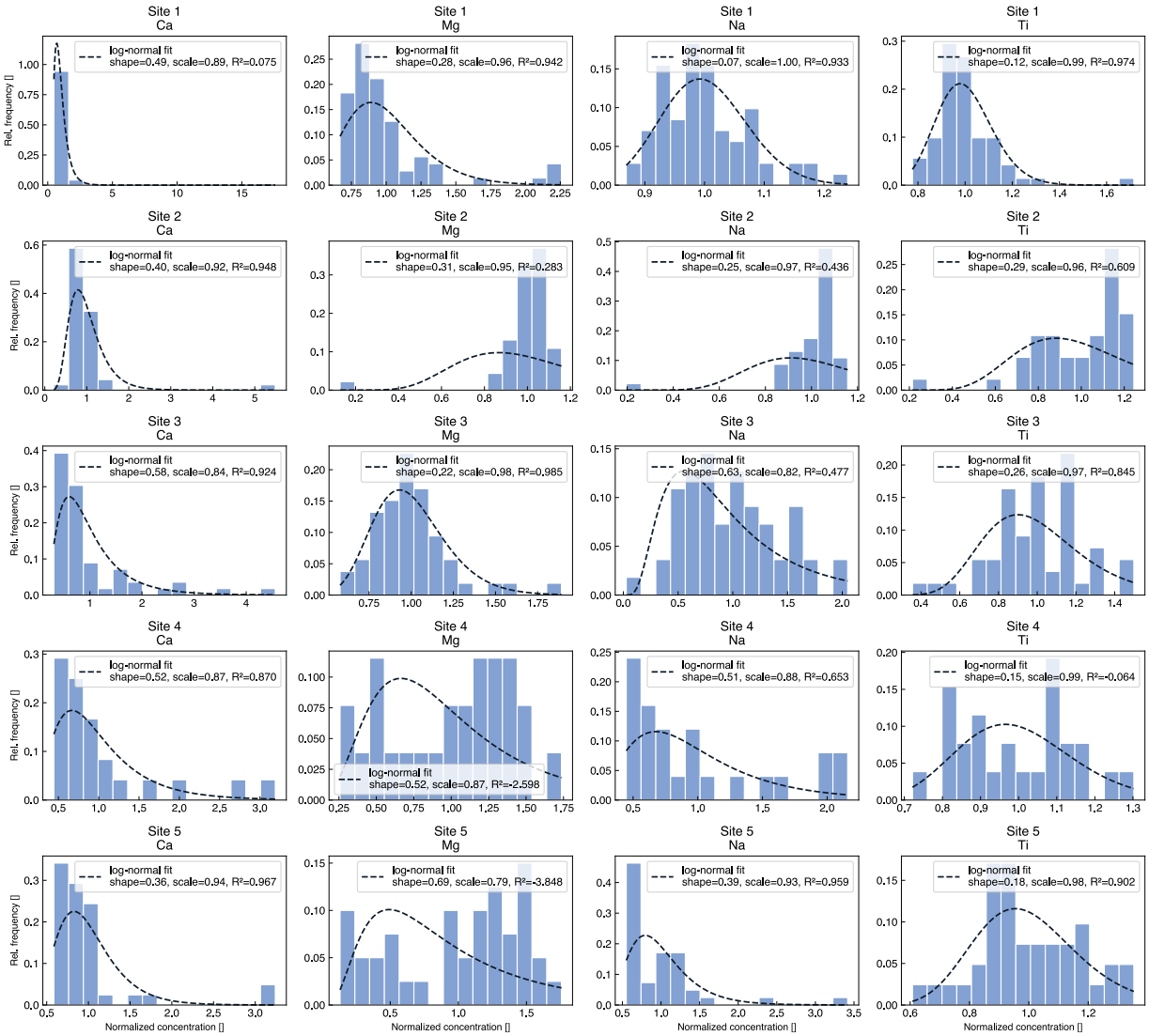

Figure S3: Distributions of baseline data for the 5 field sites (Table 1) including log-normal fits to the data. The shape parameters, corresponding to the standard deviation of the normal distribution of the logarithm of the data, are plotted in Figure S4.

Generally, a random variable is log-normally distributed if:

$$X \sim LogNormal(\mu, \sigma) \tag{S48}$$

Which means that:

$$ln(X) \sim N(\mu, \sigma^2) \tag{S49}$$

where μ is the mean, σ the standard deviation, and σ^2 the variance of the respective distributions, with log-normal distributions conventionally defined via the standard deviation of the underlaying normal distribution. The expected value (mean) of a log-normal variable X can be calculated as:

$$\mathrm{E[X]} = \mathrm{e}^{\left(\mu+\frac{\sigma^2}{2}\right)} \quad \text{S50a}$$

Hence, when using the parameters of log-normal fits to populations with a given mean (Figure S3) to generate synthetic data for the Monte Carlo simulations, if generating μ and σ independently, the mean of the resulting populations will not be the same as of the initial distribution (i.e., 1). Or said differently, if we want the mean of a synthetic distribution to be a specific value, μ and σ are not independent—only one can be randomly generated. We implement this into the Monte Carlo simulation by randomly generating shape parameters (σ_{syn}) and then calculating μ_{syn} such that $E(X) = 1$:

$$\mathrm{E[X]} = \mathrm{e}^{\left(\mu_{syn}+\frac{\sigma_{syn}^2}{2}\right)} = 1 \quad \text{S50b}$$

Now, taking the natural logarithm:

$$\ln\left(\mathrm{e}^{\left(\mu_{syn}+\frac{\sigma_{syn}^2}{2}\right)}\right) = \ln(1) \Rightarrow \mu_{syn} + \frac{\sigma_{syn}^2}{2} = 0 \Rightarrow \mu_{syn} = -\frac{\sigma_{syn}^2}{2} \quad \text{S51}$$

The empirically constrained simulated μ_{syn} and σ_{syn} describe log-normal distributions with a mean of 1 and σ (shape) parameters constrained from field data (with a mean of 1), and are used to randomly generate sets of samples by multiplying these in-field variance factors with true "true" sample compositions.

Because the σ values from the fit to field data (Figure S3) are neither normally nor log-normally distributed (negative R^2; Figure S4), in the Monte Carlo simulations we generate synthetic σ_{syn} values by randomly pulling from uniform distributions set out by the minimum and maximum

observed σ values observed in field data (for Ca, Mg, and Na the used values are 0.072402 and 0.687422, and for Ti 0.119775 and 0.288003).

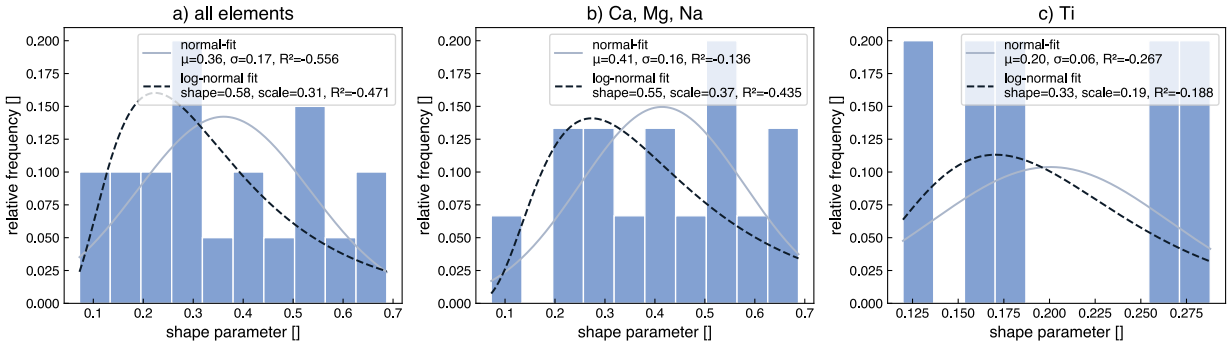

Figure S4: Histograms as well as normal and log-normal fits to the shape parameters from log-normal fits to soil data. The signal-to-noise analysis and related Monte Carlo simulations use uniform distribution set out by the minimum and maximum Ca, Mg, and Na shape values (b) as well as Ti shape values (c) due to low fit of both normal and log-normal distributions.

S3 Impact of feedstock mass loss on base cation and immobile element concentrations

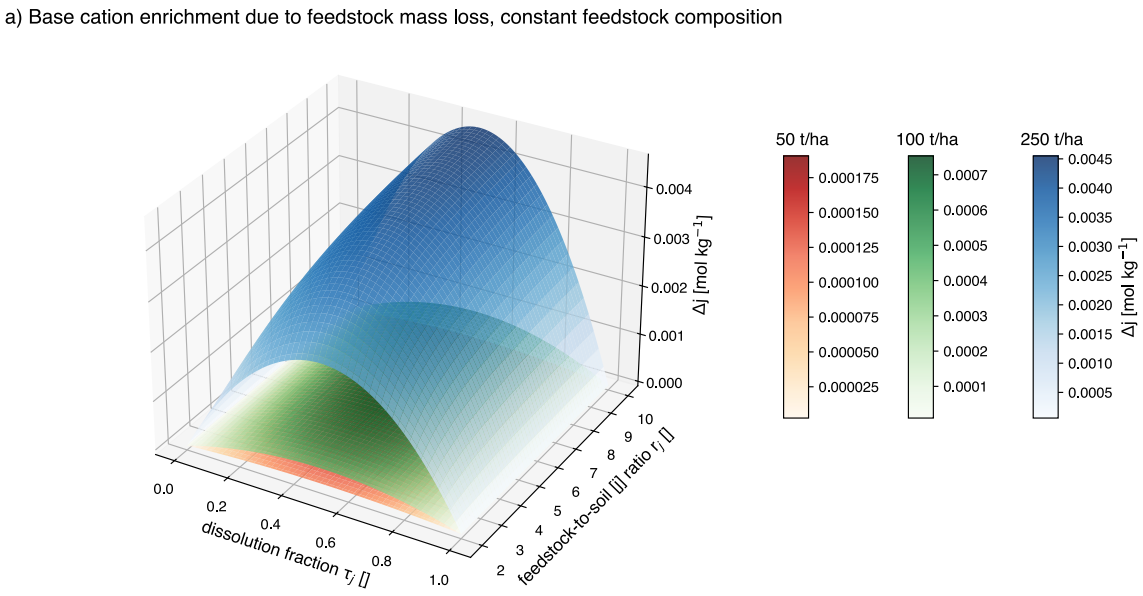

Figure S5 Change of base cation concentration as a result of feedstock mass/volume loss from the system considering constant feedstock compositions.

Calculated as:

$$\Delta j = [j]_{n=t} - [j]^*_{n=t} \quad \text{S52}$$

Where $[j]_{n=t}$ is equation from S44, and $[j]^*_{n=t}$ calculated from a linear loss of base cations relative to the dissolution fraction:

$$[j]^*_{n=t} = [j]_s + ([j]_{n=0} - [j]_s)(1 - \tau_j) \quad \text{S53}$$

Where $[j]_{n=0}$ is equation from S36.

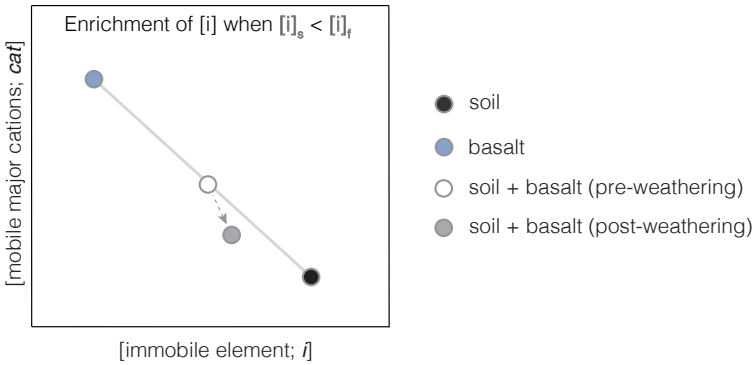

Figure S6: Sketch of the impact of enrichment of post-weathering soil immobile element concentrations when the feedstock immobile element concentration is lower than in soil.

S4 Impact of deployment parameters and soil composition on signal-to-noise analysis

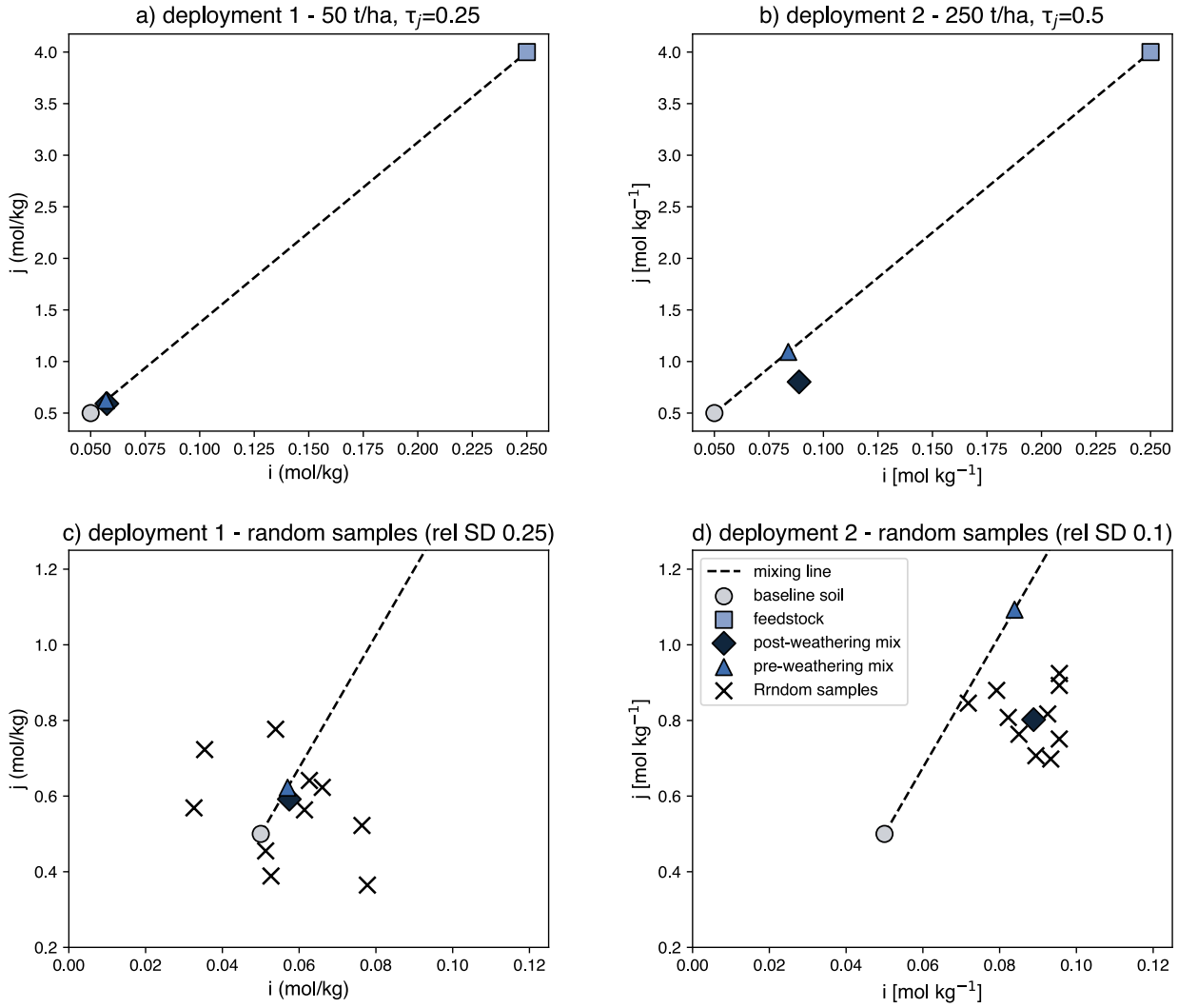

Figure S7: Two exemplary EW deployments of 50 t ha^{-1}, τ_j of 0.25 and relative 1SD on sampled soil compositions of 25% (a and c) and 250 t ha^{-1}, τ_j of 0.5 and 1SD on soil samples of 10% (b and d), representative for a low- and high- resolvability scenarios. Panels c and d show the compositions of 10 random samples generated for the post-weathering soil-feedstock mixture (exact composition and associated sample τ_j values listed in Table 2).

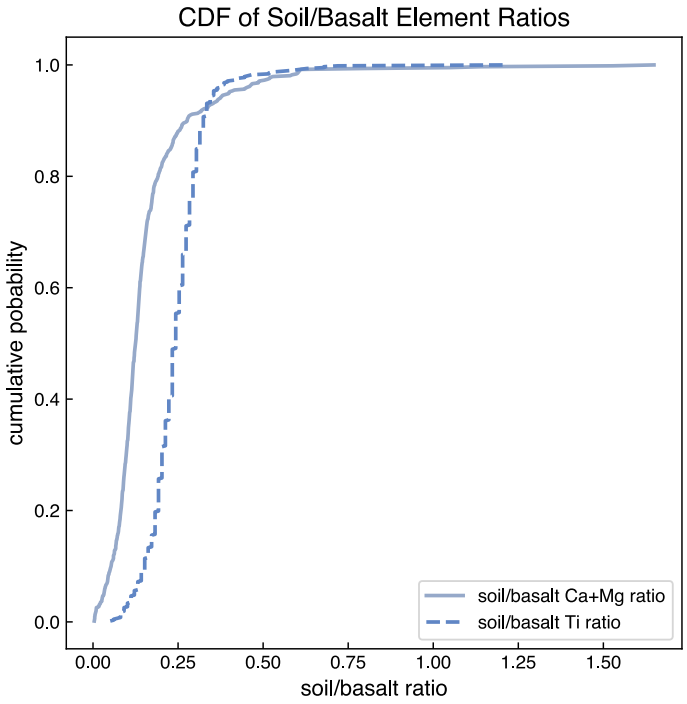

Figure S8: Cumulative distribution plot of the ratio of agricultural soil (LandCover2 = "Row Crops" and "Small Grains") composition [60] to US-basalt composition [63]. As the ratio increases above the value of 0.2 defined here as a cut off for soils suitable for SOMBA, the fraction of soils fulfilling this condition quickly increases.

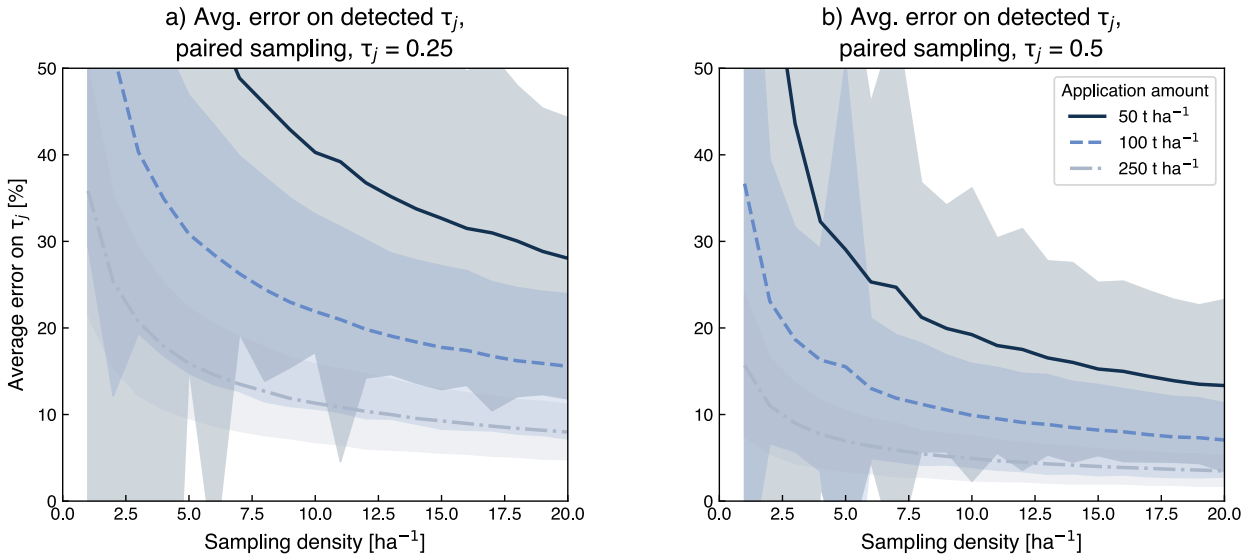

Figure S9: Average errors on detected dissolution fractions for two simulated mass transfer coefficients (τ_j = 0.25 in a, τ_j = 0.5 in b). The simulations are based on US soil [60] and basalt [63] compositions considering soils with base cation and Ti concentrations at least 2 times lower than basalt (in contrast to Figure 4, which shows the same for soil concentrations that are at least 5 times lower). The simulated in-field soil heterogeneity is based on the novel dataset presented in Table 1.